# Impact Noise Reduction in Cross Laminated Timber by Embedding Acoustic Black Holes

**Temitope Akinpelu**

**A Thesis**

**in**

**The Department**

**of**

**Mechanical and Industrial Engineering**

**Presented in Partial Fulfillment of the Requirements**

**for the Degree of**

**Master of Applied Science (Mechanical Engineering) at**

**Concordia University**

**Montréal, Québec, Canada**

**April 2024**

CONCORDIA UNIVERSITY

School of Graduate Studies

This is to certify that the thesis prepared

By: **Temitope Akinpelu**

Entitled: **Impact Noise Reduction in Cross Laminated Timber by Embedding Acoustic Black Holes**

and submitted in partial fulfillment of the requirements for the degree of

**Master of Applied Science (Mechanical Engineering)**

complies with the regulations of this University and meets the accepted standards with respect to originality and quality.

Signed by the Final Examining Committee:

_____ Chair
*Dr. Ramin Sedagahti*

_____ External Examiner
*Dr. Ghazanfarah Hafeez*

_____ Examiner
*Dr. Ramin Sedagahti*

_____ Supervisor
*Dr. Behrooz Yousefzadeh*

_____ Co-supervisor
*Dr. Joonhee Lee*

Approved by _____
Dr. Martin D. Pugh, Chair
Department of Mechanical and Industrial Engineering

_____ 2024

_____
Dr. Mourad Debbabi, Dean
Faculty of Engineering and Computer Science

# Abstract

Impact Noise Reduction in Cross Laminated Timber by Embedding Acoustic Black Holes

Temitope Akinpelu

The widespread adoption of cross-laminated timber (CLT) in building construction faces challenges, especially concerning low-frequency impact noise. Conventional methods for addressing this issue requires thick floor assemblies. This study suggests embedding acoustic black holes (ABH) into CLT floors as an alternative solution.

Functioning as a wave guide, the ABH concentrates energy in specific regions where it is absorbed by the damper. The finite-element method is used to analyze the vibro-acoustic response of CLT plates embedded with a periodic grid of ABH indentations (ABH-CLT). The goal is to evaluate the influence of the outer radius, number of indentations, and structural damping on the vibro-acoustic response within 50-800 Hz and assess reduction in radiated sound power.

The structural response shows that including ABH in CLT floors leads to unintended resonance frequencies. However, characterizing these changes is challenging due to other influential variables. Likewise, varying the number of indentations does not show a clear trend in radiated sound power at a loss factor of 0.03. However, with a higher loss factor (0.2), the trend favors maximizing the indentations.

Increasing the outer radius shifts the structural response to lower frequencies, but the acoustic response remains unpredictable at a loss factor of 0.03, suggesting that the amount of damping is more influential this frequency range.

In the third-octave band, ABH-CLT consistently attenuates sound power levels at higher frequencies above 400 Hz, which is equally achievable by damping a CLT without ABH. However, the ABH is not effective in mitigating impact noise below 400 Hz.

# Acknowledgments

I would like to express my gratitude to my family for their unwavering support throughout this journey. Their encouragement, understanding, and sacrifices have been invaluable to me.

I am also immensely thankful to my supervisors, Dr. Behrooz Yousefzadeh and Dr. Joonhee Lee, for their guidance, expertise, and patience. Their insightful feedback, encouragement, and mentorship have been instrumental in shaping my academic journey.

# Contents

# List of Figures

# List of Tables

# Chapter 1

# Introduction

## 1.1 Performance of Cross-Laminated Timber

The growing demand for mass timber in building construction can be attributed to its reputation as a more eco-friendly alternative to traditional building materials such as steel and concrete. Notably, the proportion of non-residential structures employing wood-framing has risen from 28% in 2016 to 34% in 2020 [35]. Recent updates to building codes have incorporated multi-story wooden construction methods [29], [34].

Cross-laminated timber (CLT) is a type of engineered mass timber panel that is gaining strides as the preferred option in building construction for residential and commercial usages [31]. It is made by stacking multiple layers of timber panels in alternating directions and then bonding them together using structural adhesives. The resultant composite panel is lightweight, yet structurally robust and fire-resistant. However, the combination of its low mass and high stiffness results in poor acoustic insulation performance, especially in the low-frequency regime. Studies have reported building occupant dissatisfaction concerning low-frequency impact noise, despite these constructions complying with present noise regulations [29], [40]. A contributing factor to this discrepancy lies in the direct application of standardized impact sound assessments on wooden structures, which were originally tailored for heavier constructions such as concrete. This results in a mismatch compared to subjective ratings provided by occupants. Fortunately, the growing popularity of CLT has brought motivation for and interest in understanding how to mitigate low-frequency impact noise in

these materials.

One research direction is to characterize the structural and acoustic properties of CLT. Obtaining the material properties of wood presents a challenge due to variations in the macroscopic and microscopic structure over several wood species, compounded by a lack of comprehensive databases and uncertainties induced during manufacturing [29], [38]. As a result, experiments are used to calibrate deterministic models developed using analytical expressions [28] or numerical methods like Finite Element Analysis (FEA) [29], [38]. This process is typically carried out on a case-by-case basis.

Another research direction centers on exploring sound insulation treatments that can be implemented during construction. Examples of such treatments include floating floors, resilient ceiling mounts, and active or semi-active damping [40]. Nevertheless, these solutions prove insufficient in mitigating impact noise within the low-frequency range, which can require a complex construction assembly [40]. The challenge still lies in the fact that the effective stiffness or mass that CLT panels possess at low frequencies cannot create enough resistance to be effective at long wavelengths.

In light of these challenges, recent advancements have explored treatments that can be integrated into the manufacturing process of CLT panels to address low-frequency impact noise. Gibson et al. [40] proposes the use of acoustic metamaterials which are engineered substructures designed to absorb wave energy at specific frequencies. These substructures can then be tailored to address frequencies of interest. This work proposes the use of Acoustic Black Holes (ABH) on CLT panels.

## 1.2 Acoustic Black Holes (ABH)

Originally proposed by Mironov in his seminal work [2], the principle of operation of an ABH is rooted in the natural properties of retarding structures. Mironov showed the possibility of achieving a nonreflecting or fully absorbed flexural wave traveling through a beam that is terminated by a wedge with power-law decreasing thickness profile as illustrated in Figure 1.1. Ever since, the subject has attracted growing interest in the structural dynamics and vibro-acoustics communities as a potential measure for passive vibration control.

Assuming an ideally tapered wedge (one with the thickness vanishing at the end of the wedge), the velocity of the incoming flexural waves gradually decreases, ultimately leading to a fully trapped,

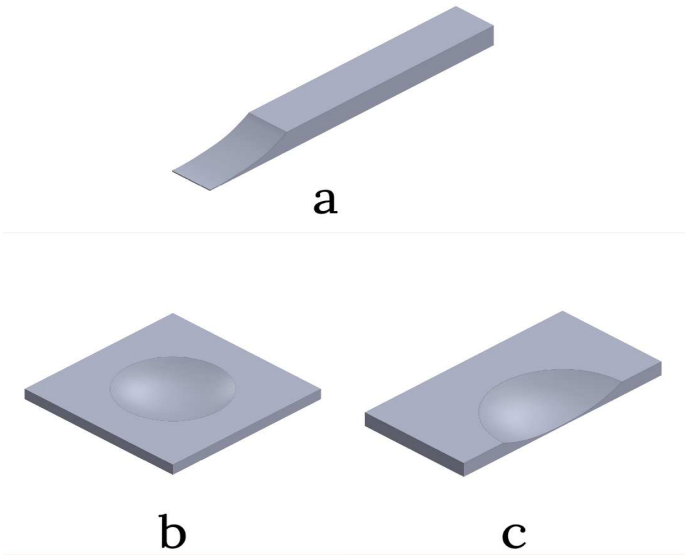


Figure 1.1: Decreasing thickness profile in an (a) ABH beam ang (b-c) plate.

non-reflected wave. Equally, the particle displacement at the tip of the wedge grows unbounded, creating a point of singularity. Nonetheless, achieving a wedge with zero thickness is not feasible in practice, and a residual thickness will exist. Mironov [2] further showed that even a very thin residual thickness has a detrimental effect on structural performance because it can significantly increase the reflection coefficient. This challenge can be addressed by including a light dissipative layer in the retarding region. Although a perfect zero reflection coefficient may not be achieved, the inclusion of a dissipative layer can significantly reduce the reflection coefficient when compared to a beam without an embedded ABH.

The ABH concept was extended to plates by Krylov [5]. By embedding axisymmetric circular indentations with power-law decreasing thickness, similar responses as those observed in beams led Krylov to coin the term “acoustic black holes”, drawing an analogy with optical black holes. Subsequently, various configurations of the ABH have been studied to investigate their effectiveness in reducing vibration and impact noise, with some proposals in acoustic metamaterials where the material properties in a composite materials are varied according to the power law profile [10], [36]. Figure 1.1b illustrates an ABH plate with an axisymmetric circular indentation in the middle. Figure 1.1c illustrates the cross-section of the ABH plate highlighting the semblance in retardation

as found in ABH beams.

## 1.3 Sound Radiation in Structures

Sound radiation is a fluid-structure coupled problem governed by boundary interactions between the surface vibration of the structure and surrounding air pressure. The fluid pressure creates surface traction on the structure, while the acceleration in the structure creates pressure traction on the fluid boundary [11]. In many cases, the structural response dominates in the coupled study and drives the fluid to radiate sound. The fluid loading can also be strong enough in some cases so as to drive the structural response as in the case of blast loading such as an explosion.

The flexural wave velocity of a beam is directly proportional to the thickness of the beam. Thus, in an ABH beam where the thickness gradually decreases to zero, the corresponding wave velocities also decrease to zero. Thus the sound radiated from the structure will decrease. Studies have shown reduced sound radiation when ABHs are integrated into plates and beams. [12], [28], [36].

## 1.4 Scope of Study

This study explores the possibility of reducing low-frequency impact noise in CLT panels by embedding ABH. It is expected that the vibro-acoustic properties of the modified CLT panel will depend on several factors such as the size of the panel, the size of the ABH regions and number of ABH indentations. Currently, there is no definitive guide on sizing the ABH indentations in a CLT panel.

Using the Finite Element Method (FEM), this study conducts a parametric analysis to assess the vibro-acoustic behavior of CLT panels within the frequency range of 50-800 Hz. The investigation systematically varies the outer radius of the ABH region and the number of indentations. Under the same loading conditions, the trends of mobility and radiated sound power level of panels with and without ABH indentations are compared. The aim is to determine the frequencies at which sound power reduction can be achieved by incorporating ABH.

## 1.5 Thesis Outline

The thesis report follows the following structure:

(1) Chapter 2 presents an integrated topical literature review, covering topics such as sound radiation in plates, numerical modelling of CLT and the state of the art on ABH.

(2) Chapter 3 outlines details of the numerical model and procedure setup for the parametric study.

(3) Chapter 4 offers an in-depth analysis of the vibro-acoustic performance of the CLT panel with and without ABH and relates it the geometric variations.

(4) Chapter 5 concludes the thesis by summarizing the key contributions, main findings, and recommended directions for future studies.

# Chapter 2

# Literature Review

## 2.1 Introduction

Mass timber panels are becoming increasingly popular in multistory construction thanks to advancements in timber engineering and updates to national building codes [31], [40]. These panels, which are extensively prefabricated, offer environmentally friendly alternatives to conventional materials like steel and concrete. However, their low mass and high stiffness result in subpar acoustic performance, especially when exposed to high-energy, low-frequency impact forces such as those caused by human footsteps.

Cross Laminated Timber (CLT) is an engineered mass timber product created by stacking multiple layers of wood in alternating directions, bonded with structural adhesives. This layering technique results in a composite panel with adequate stiffness in all directions. However, despite the additional layers, the overall mass-to-stiffness ratio remains relatively low, which presents a persistent challenge for acoustic performance.

While existing building codes often classify timber buildings as having good acoustic performance, research indicates significant discrepancies between standard ratings and dissatisfaction expressed by building occupants [40]. One contributing factor to this discrepancy is the direct application of codes originally designed for traditional building materials to wooden structures.

Current impact sound insulation technologies include floating floors, mass toppings, resilient

ceiling mounts, and insulation fillings. Practical solutions involve a combination of these technologies to improve sound absorption by increasing the mass and isolating vibration within the floor assembly. The National Research Council Canada (NRC) reports a 15 dBA improvement in Impact Insulation Class (IIC) when a 38mm thick concrete layer floating on a 10mm tar board is added to a 5-ply, 175mm CLT floor [13]. Additional 18 dBA improvement can be achieved by further incorporating a suspended ceiling with rockwool fillings [13]. Nevertheless, these methods typically prove ineffective at mitigating low-frequency impact noise. The challenge arises from the high mass and stiffness required to resist high-energy low-frequency inputs or the lack of impedance discontinuities to manipulate bending waves. A detailed discussion of the physics of impact noise is presented in Section 2.3.

Challenges in achieving effective low-frequency attenuation have motivated research on changes that can be integrated into the mass timber panel during the manufacturing process. One approach involves the use of acoustic metamaterials, as proposed by Gibson et al. [40]. This project explores the integration of embedded Acoustic Black Holes (ABH) within cross-laminated timber. Starting with a comprehensive review of the physics of impact noise and literature pertaining to the impact sound insulation performance of CLT, this chapter offers an integrated literature review covering numerical modelling of CLT, the principle of operation of ABH, the state of the art on ABH technology, and numerical modelling of ABH.

## 2.2 Acoustics of a Floor Panel

### 2.2.1 Sound Transmission through Floors

Before delving into the various mechanisms through which sound travels within buildings, it is crucial to establish the underlying physics governing the interaction between a vibrating panel immersed in a fluid (with focus on air as the fluid medium). Sound propagation through panels arises from the interaction between bending waves within the panel and acoustic waves within the fluid medium. Bending waves are flexural waves caused by transverse displacement on the panel's surface while acoustic waves are longitudinal waves originating from the repetitive compression and extension of fluid molecules originating from the movement of the panel's surface. The bending

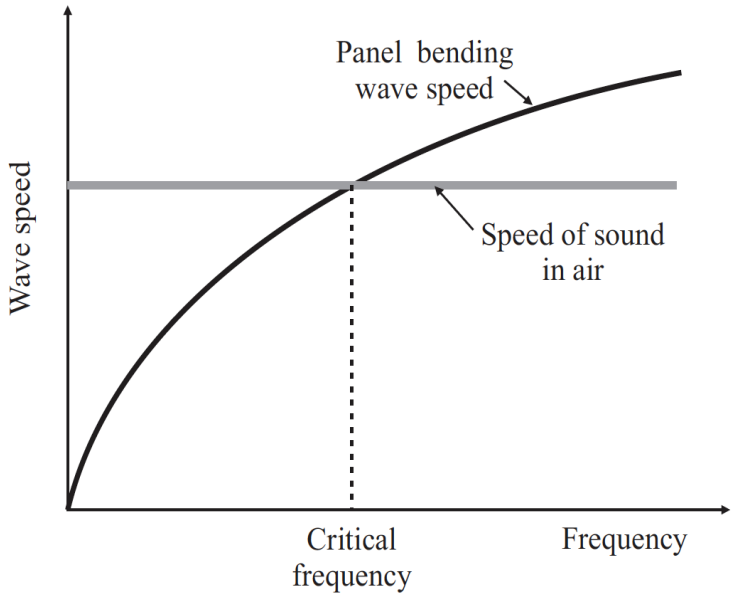


Figure 2.1: Illustration of critical frequency [24]

wave speed, $c_B$, of an isotropic panel can be expressed as:

$$c_B = (B\omega^2/m)^{1/4} \tag{1}$$

where $\omega$ is the angular frequency, $m$ is the panel mass and $B$ is the bending stiffness [24].

In the case of a panel vibrating within a fluid, there is a *critical frequency* at which the speed of sound in the fluid matches the bending wave speed of the panel. This condition establishes the prerequisite for sound to radiate efficiently into the surrounding fluid medium. The critical frequency, as defined below [24]

$$f_c = \frac{c^2}{2\pi}\sqrt{\frac{m}{B}} \tag{2}$$

Below the critical frequency, the bending and projected acoustic wavelengths are unequal, resulting in weak fluid-structure coupling, hence no sound radiation. However, about the critical frequency, the fluid-structure coupling becomes more pronounced, leading to strong sound radiation from the panel. This phenomenon is commonly employed to assess the insulation capabilities of a panel.

Radiation efficiency, $\sigma$, is used to quantify how well structure-borne sound waves are radiated to sound waves in the adjacent fluid. It is defined as the ratio of radiated power by the panel to available power. The available power may be seen as the power radiated by a large baffled piston with uniform mean-square velocity equal to the temporal and spatial average mean-square velocity of the panel [7]

$$\sigma = \frac{W}{S\rho_0 c_0 \langle V_{t,s}^2 \rangle} \tag{3}$$

where $W$ is the radiated sound power, $S$ is the panel surface area, $\rho$ is the fluid density and $c_0$ is the speed of sound in air. Assuming the panel is baffled on one side, the radiated sound power can be expressed as [7]

$$W = \frac{1}{2} \int_S \Re[pv^*] dS \tag{4}$$

where $p$ is the radiated sound pressure and $v^*$ is the complex component of the particle velocity that is perpendicular to the panel surface.

In a continuum, the integral can be straightforward to accomplish, recognizing that the radiated pressure and fluid particle velocity can be directly related to the lateral component of the bending wave velocity in the panel at all points across the acoustic-structural interface. See Hopkins [7] for an expanded discussion on the complete formulation. However, in a finite element model, extracting the radiated power needs some adjustments, especially in the case of a non-uniform mesh, this technique is further discussed in section 3

Sound fields radiated by the panel in the receiving room are contingent on the nature of the excitation in the source room, which can either be an incident acoustic wave (as in the case of a speaker in a room) or a mechanical force (as in the case of impact force on the floor). Both types of excitation are elaborated in the following section.

### 2.2.2 Types of Sound Transmission

#### Airborne Sound Transmission

Airborne sound transmission within a building originates in the source room, in the form of an incident acoustic wave generated by speakers or people talking. This sound propagates into the receiving room, traversing through various pathways such as wall or floor partitions, air gaps, and pipes. However, for the sake of standard calculations, our discussion will focus primarily on transmission through partitions.

The Transmission Loss (TL) quantifies the fraction of sound energy that is transmitted through a partition, considering that some of the sound is also reflected and absorbed by the wall. It is determined by measuring and calculating the difference in the space-averaged sound pressure level between the source room and the receiving room, which are separated by a partition. The following equation is used to evaluate the TL.

$$TL = -10 \log_{10} \tau \tag{5}$$

where $\tau$ is the transmission coefficient.

Single-number ratings are employed to characterize the air-borne sound transmission loss of different partitions. The commonly used ASTM E413-16 defines the Sound Transmission Class (STC) for a partition by applying curve fitting to measured Sound Pressure Level (SPL) data within 1/3-octave bands, a higher STC rating indicates better insulation properties of a partition [17]. Likewise, ISO 717-1 defines a Weighted Sound Reduction Index ($R_w$) for a partition, using similar curve fitting techniques with slight variations in criteria [32].

#### Impact Sound Transmission

Impact sound arises when partitions are mechanically stimulated by forces such as footsteps. Vibrations propagate through the panel until they excite the panel's surface in direct contact with the air of the receiving room. The conditions for sound radiation in the receiving room are determined by the critical frequency, as discussed in section 2.2.2, which is also influenced by the physical dimensions of the panel.

Impact noise isolation quantifies a partition's ability to prevent noise transmission resulting from impact forces. It is determined by measuring the space-averaged sound pressure level in a receiving room due to the impact force generated by a standard tapping machine on the partition separating the source and receiving rooms. The normalized impact sound level ($L_n$) is subsequently calculated using Eq. 4.

$$L_n = L_p + 10log_{10}(S\overline{\alpha}/10) \tag{6}$$

Similar to airborne transmission loss, single-number ratings classify the impact isolation performance of a partition. ASTM E989-06 defines the Impact Insulation Class (IIC) as a single number rating [6], while ISO 717-2 defines a Weighted Normalized Impact Sound Pressure Level ($L_{nw}$) [33]. A higher numerical value signifies better insulation performance. Both methods are calculated in a manner similar to STC, involving a curve-fitting technique applied to Ln values obtained during measurement. Detailed calculation procedures can be found in the respective standards, and readers are encouraged to consult them.

The effectiveness of a partition in mitigating airborne or impact disturbances is influenced by a multitude of factors, including but not limited to the material used, the nature of the noise source, floor interconnections, soundproofing measures, and vibration isolation treatments. For example, studies have shown that the energy transmitted to the floor can vary based on factors such as the walker's mass, footwear type, and the location of the impact [15]. With a specific focus on impact noise disturbance, the following section delves into some of the contributing factors that influence the performance of wooden structures when subjected to impact forces.

## 2.3 Impact Noise in Wooden Structures

Mass timber products are steadily gaining favor as the go-to construction material for both residential and commercial buildings. Cross Laminated Timber (CLT) is a type of engineered mass timber product that is made by stacking multiple wooden panels in alternating directions and bonding them together with structural adhesives to form a composite wood structure that is both lightweight and structurally robust. Despite being heavier than single layer timber floors, the resulting panel still

exhibits the common acoustic performance issues associated with wooden structures, particularly at low frequencies.

The National Building Code of Canada provides impact sound ratings for certain wooden floor assemblies, serving as a reference for acousticians during the design process [34]. Many of these assemblies achieve an IIC rating ranging from 40 to 50, while some intricate assemblies can even reach up to 70. However, it is important to note that standard impact sound tests, such as ASTM E989-06 and ISO 717-2 may not provide accurate assessments for the performance of timber floors, particularly at low frequencies. Several reasons for this limitation are outlined.

(1) The tapping machine, originally developed for concrete floors, has low mass and generates low-energy impact disturbances in the source room. This fails to accurately replicate the impact of heavy human footsteps on lightweight floors [15], [19]. The walking force spectra in Figure 2.2 show high concentration of energy at low frequencies compared to the spectra produced by a tapping machine. While the study does not investigate the corresponding impact sound produced as a result of the force profile, it underscores the need to contemplate using alternative impact sources. For example, the ISO-standardized rubber ball has shown an improved correlation with human footsteps. Certain standards, such as JIS_A_1418-2 [26], have adopted the use of rubber balls as impact sources.

(2) Sound pressure levels are assessed in the room below over a broad frequency range, typically spanning from around 100 Hz to 4000 Hz, although there are also low-frequency adaptations ranging from 50 Hz to 2500 Hz. Weightings are subsequently applied to generate single-number ratings that serve as benchmarks for the floor performance. However, this approach, which optimizes over a wide frequency spectrum, may not effectively convey performance expectations at narrow frequency bands within the low-frequency range. This is why standards like JIS_A_1418-2 [26], concentrate on 50 to 630 Hz range and introduce the single-number rating index $L_{Fmax}$ to address this frequency region.

(3) The complex interaction between impact sources and the floor at varying frequencies creates distinct acoustical responses across different materials. This nuanced behavior is not fully captured by the broad-frequency evaluation employed in standard methods. For example, a

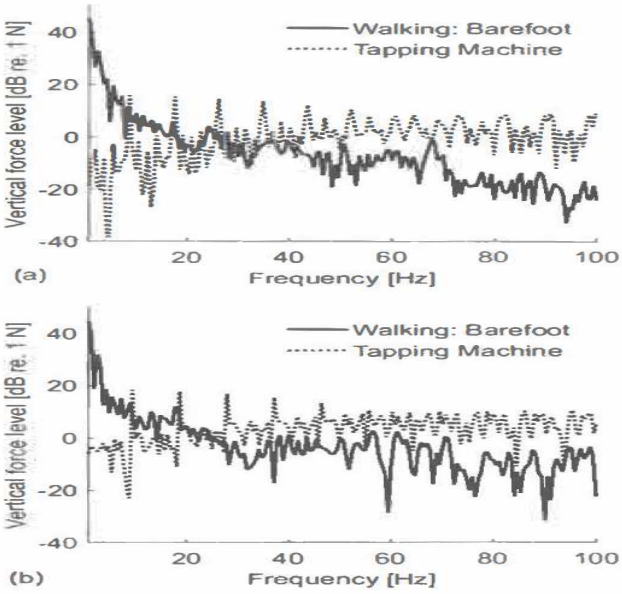


Figure 2.2: Tapping machine vs. walking force spectra on (a) wooden floor, (b) cement-wood floor [15]

cement floor experiences little difficulty in attenuating low-frequency noise regardless of the impact source due to its high mass. In contrast, a wooden floor faces challenges in this low-frequency range. However, both types of floors exhibit similar performance in the mid- to high-frequency range. Consequently, when acoustic treatments are applied, they may yield acceptable standard ratings, even though cement and wood demonstrate different behaviors in the low-frequency range. Figure 2.3 illustrates the impact sound spectra within the 20 Hz to 800 Hz range generated by a 70 kg person walking on both timber and concrete floors. These spectra are compared against the human hearing threshold, which is also indicated. The disparities between the timber spectrum and the hearing threshold offer insight into why there is a mismatch with perceived satisfaction from building occupants.

### 2.3.1 Current Insulation Technologies

The fundamental challenge in attenuating impact noise in wood flooring stems from the lack of inertial and stiffness resistance to impact forces at specific frequencies. Ideally, floor assemblies with lower natural frequencies or higher modal densities are sought after. Current insulation

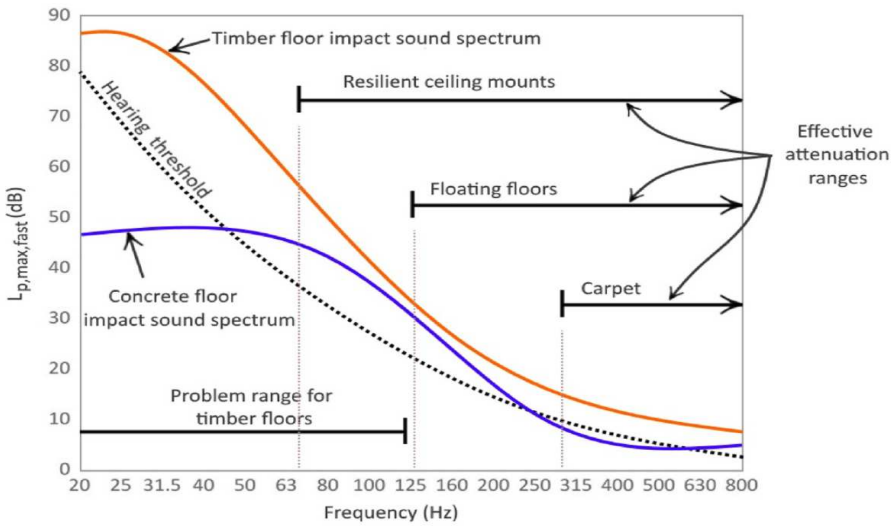


Figure 2.3: Impact sound spectra produced by 70kg man walking with socks with indicative hearing thresholds and effective attenuation frequency ranges for different attenuation technologies [40]

treatments address this challenge by either increasing the mass of the floor assembly or utilizing vibration isolation techniques. In most practical solutions, a combination of these strategies is employed. Figure 2.4 illustrates sound insulation assemblies applied to timber floors. In Figure 2.4a, only floor finishes and acoustic products are directly applied to the timber floor, which could be in the form of a rubber-type inter-layer between a rug and timber floor. In Figure 2.4b, a mass topping such as concrete is added to increase the overall mass of the floor assembly. Zhao conducted an extensive study on the influence of floating concrete toppings with elastic inter-layers on timber floors, utilizing the standardized Impact Insulation Class (IIC) as defined by ASTM [31]. Higher IIC ratings tended to be associated with thicker concrete toppings and elastic inter-layers with lower dynamic stiffness. Despite these treatments, it remained challenging to achieve IIC benchmarks of 55, supporting the NRC's assertion regarding the limited insulation enhancement provided by floating concrete [8]. It is worth noting that floor assemblies with concrete toppings did enhance acoustic performance when compared to the timber floor without concrete toppings.

In Figure 2.4c, discrete floor block mounts are introduced to isolate vibrations, resulting in lower natural frequency for the floor assembly. Discretely raised floors tend to achieve higher Impact Insulation Class (IIC) ratings more readily compared to the previous configurations [20], [31], and the

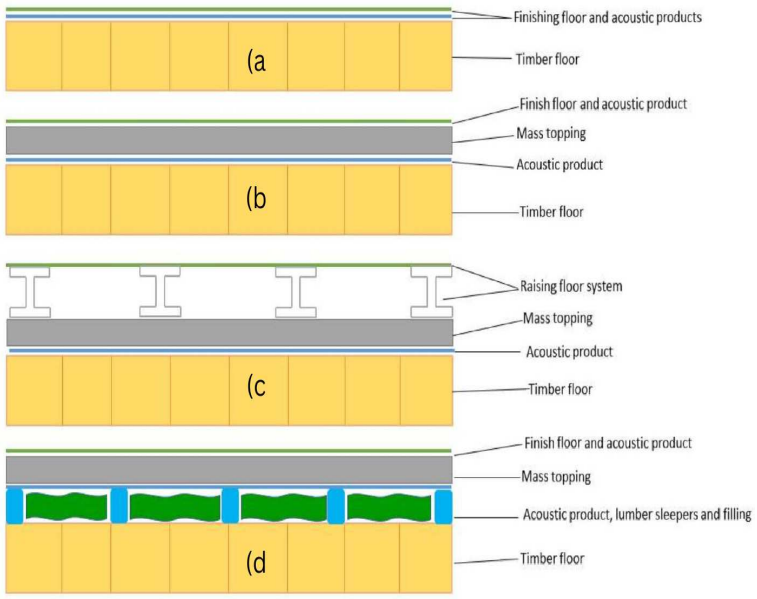


Figure 2.4: Some sound insulation technologies [31]

reasons for this improvement are closely related to discontinuities introduced at discrete points, acting as barriers to hinder the transmission of bending waves by reflecting them. Zhao demonstrated that by incorporating raised floors with mass toppings, elastic inter-layers, and rockwool fillings, IIC ratings of up to 65 were achievable [31]. However, there remains a concern regarding the path of those reflected waves; they may contribute to flanking noises, especially in scenarios where walls and floors are interconnected in real building structures. It is worth noting that standardized impact tests typically prioritize the reduction of flanking noise in the setup, potentially deeming further investigation into flaking noise unnecessary.

The mathematical model of a floor assembly can also affect analysis of the results. In Zhao, the elastic inter-layers are evaluated using dynamic stiffness as a parameter [31]. However, the elastic layers, concrete, and wood also possess inherent damping characteristics that allow them to dampen out oscillations over time. Consequently, they can be equally modelled as spring-dampers, and the damping factor can become a crucial parameter when designing floor assemblies that guides the selection of appropriate inter-layers.

Integrating ABHs into CLT panels offers the possibility of incorporating particle dampers such as sand, sawdust, and granulated rubber into the voids of the Cross-Laminated Timber (CLT) for

enhanced damping [42]. In addition, given that the current combinations of insulation treatments reduce the overall room clearance, the incorporation of ABHs can assist in achieving equivalent IIC ratings while potentially requiring less space.

### 2.3.2 Standard Impact Noise Assessments and Occupant Satisfaction

When assessing performance in the low-frequency range, achieving satisfactory results with current insulation treatments remains a complex challenge. For example, Zhao has conducted an evaluation of low-frequency impact performance in accordance with JIS 1418-2 and reported $L_{Fmax}$ ratings for some assemblies that displayed significant distinctions in their IIC ratings [31]. However, the precise implications of these $L_{Fmax}$ ratings are not entirely clear.

The question of whether a reported rating implies "acoustic comfort" or not has been the subject of numerous studies [3], [13], [21]. The correlation between sounds produced in the low-frequency range and building occupant satisfaction is still in its nascent stages, with multiple subjective studies underway to establish links between numerical ratings and human perception. Moreover, these studies face various challenges due to human individuality which fall within the domain of psychoacoustics, making it a scientifically complex area to explore.

One category of correlation studies aims to establish connections between measured sound pressure levels and acoustic surveys based on subjective perception of sound disturbance. These studies have revealed that impact sound is perceived as more annoying in timber buildings compared to concrete buildings [40]. Examining mass psychology through the large surveys can provide a foundation for defining what is considered acceptable in terms of noise levels. For instance, a socio-acoustic survey conducted by Rindel [18] on 600 homes in Norway found that the percentage of satisfied occupants decreased from 85% to 18% as the sound pressure level increased from 45 dB to 65 dB, particularly around 50 Hz. However, it is important to note that cultural differences can slightly affect the generalization of these results. A recent study by Mueller et al. reported variations in perceived acoustic performance satisfaction of wood structures in different countries [41].

Another category focuses on establishing relationships between standardized impact tests and acoustic surveys based on subjective perception of sound disturbance. For instance, Bodlund [1] found that this correlation increased from 74% to 87% when the data at 50 Hz was included in

the surveys. This improved correlation was achieved by modifying the curve weighting in the ISO standard procedure. It is worth noting that altering the weighting curve detaches from the ISO standard procedure for calculating single-number impact ratings. This argument is applicable to other studies that have explored modifying the weighting curve to enhance correlation with human perception. Above all, there is a consensus regarding the importance of including low frequencies to more accurately reflect occupant satisfaction levels, emphasizing the need for standardized tests in the low-frequency range [40].

In summary, it is evident that defining low-frequency impact noise performance criteria for timber structures in terms of standardized impact ratings is a challenging task. This project does not aim to quantify improvements in the acoustic properties of the wood structure solely based on standardized impact evaluations. Instead, the results will investigate whether there is improvement in the vibro-acoustic performance of CLT panels with acoustic black holes compared to CLT panels without ABH indentations, with emphasis on the low-frequency range.

## 2.4 Numerical Modelling of Cross Laminated Timber

Predicting the dynamic behavior of wood is challenged by several factors. Firstly, wood is an orthotropic material, which means that its elastic properties differ along perpendicular planes of symmetry. This complexity introduces three parameters that need to be determined experimentally, compared to homogeneous materials that require only one parameter (Young's modulus). Furthermore, the variation in wood species across locations causes differences in microscopic structures within the wood [29], [38]. As a result, vibro-acoustic studies conducted on wood often specify the particular wood species under investigation.

The Finite Element Method (FEM) is a widely employed numerical approach for predicting the dynamic behavior of structures especially in cases where the analytical solution is difficult to obtain. It does this by discretizing an integral domain into finite elements through an interpolation function [11]. The resulting system can be arranged into mass, stiffness and damping matrices which are used to compute responses such as eigen frequencies and deflections, a summary of the formulation is discussed in section 2.8

The FEM allows for the reduction of experimental tests, leading to time and cost savings, and facilitates parametric studies. However, when dealing with wood, predicting its response remains a laborious and time-consuming process. The lack of developed material database for wood is a contributing factor [29]. Consequently, a significant amount of effort is often dedicated to calibrating the numerical model to align with an existing experimental model before further investigations can be conducted. Before calibration, material properties of the wood are typically gathered from existing literature to establish a baseline for the numerical model, and then the dynamic responses are compared with those of an experimental setup. Hence, the primary objective of calibration is to achieve the highest possible correlation between the dynamic performance of the numerical model and the experimental model. This correlation can be established through various methods. For instance, Qian et al. [29] employed a stochastic approach to address uncertainties arising from material properties in a specific CLT floor configuration. The aim of their simulation was to optimize the shear moduli and Young moduli to minimize the Normalized Relative Frequency Difference (NRFD) between the measured and simulated natural frequencies of the CLT floor. Their optimization procedure was primarily focused on the low-frequency range and was able to achieve a strong correlation up to 100 Hz. For additional details on the constraints injected into the optimization process, the reader is referred to Qian et al. [29]. In contrast, Yang et al. [38] conducted a sensitivity analysis using the diffuse field transmission loss of the CLT panel as a target to explore the uncertainties related to Young's and shear moduli. While this was not an optimization study, it provides insights into how different optimal material property values can be achieved depending on the constraints used in optimization. Unlike the frequency response sensitivity analysis obtained by Qian et al., Yang et al. found transmission loss to be more sensitive to Young's modulus in one of the longitudinal directions and to shear modulus in the vertical direction [29], [38].

CLT can be modeled in various ways, with certain limitations determined by factors such as the domain size and available computational resources. Commercial finite element (FE) software provide a range of elements tailored to specific needs. The recommended method for modeling CLT involves using solid elements, orienting their material properties as they would be in a practical CLT assembly, as illustrated in Figure 2.5. Solid elements offer the advantage of capturing through-thickness modes, which contribute to structure-borne sound and might be missed when using shell

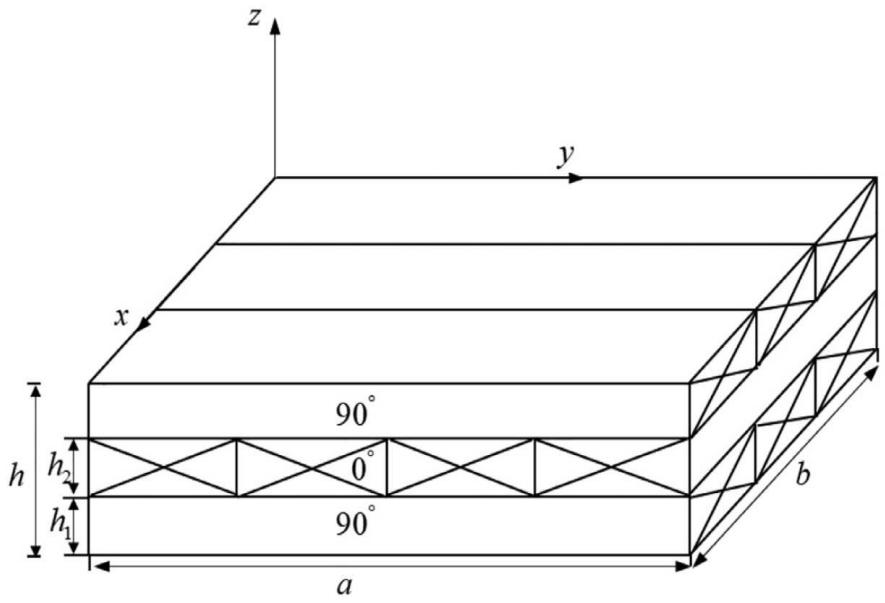


Figure 2.5: Three-layer CLT FE model with layer thicknesses h1, h2 , length a, and width b, and ply angles $90°/0°/90°$ [38]

elements or even single-layered equivalent solid elements.

In a study conducted by Yang et al. [38], a CLT panel modeled with single-layer solid elements, multilayered solid elements, and single-layer plate elements showed similar structural responses at low frequencies, exhibiting three wave branches: bending, shear, and in-plane waves. The computed branches began to diverge at higher frequencies, primarily due to the contributions from through-thickness modes, with shell elements showing the largest divergence due to the thinness assumption in its formulation.

While using solid elements can be advantageous, it also introduces specific complexities to the analysis. For instance, accurately modeling a pinned boundary condition can pose challenges. Conversely, conducting experiments to achieve a fixed-fixed CLT panel can be both costly and time-consuming. Yang et al. adopted a compromise by employing Wave and Finite Elements (WFE) [38]. This approach assumes an infinite domain, thus avoiding the necessity for boundary conditions. While Qian et al. modeled a pinned boundary condition in their study, capturing frequencies that were not observed during their experiment [29]. In summary, boundary conditions can impose limitations on the study.

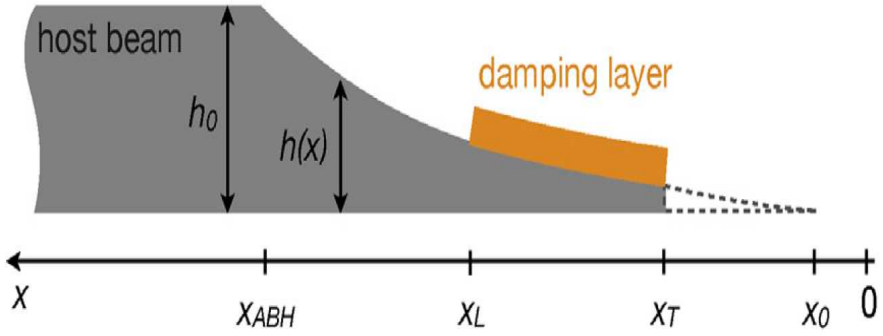


Figure 2.6: Practical implementation of the ABH profile with truncated terminus and viscoelastic damping layer [36].

Solid elements are chosen to model CLT panels in this work. The choice was primarily influenced by the incorporation of acoustic black holes. The use of solid elements is prevalent in the literature for this purpose. In addition to their ability to capture through-thickness modes in CLT, solid elements offer flexibility in creating complex geometries. Although the boundary condition for the numerical model will be left free, deviating from a realistic setup, this approach has been widely used in the literature [12], [27]. It simplifies the analysis of the acoustic black hole effect. When seeking correlation with experimental data, boundary conditions must be carefully considered for both the experimental and numerical models.

## 2.5 Acoustic Black Holes

The Acoustic Black Hole (ABH) is a passive vibration control technique that has been developing in recent years. Unlike existing methods, the ABH brings a unique advantage by reducing the total mass of the structure. This property can be beneficial in engineering applications aiming to create structures that are both durable and lightweight. The operating principle of an ABH is based on the natural properties of retarding structures. Using an analytical approach, Mironov [2] demonstrated the possibility of achieving a non-reflecting or fully absorbed flexural wave traveling through a beam that is terminated by a wedge with a power-law decreasing thickness profile, as shown in Figure 2.6.

Practical implementation of the ABH still involves the application of a damping material. However, the amount of damping material required is significantly reduced compared to what would be needed in an equivalent structure without an ABH. The following section elaborates in detail the operating principles of an ABH.

### 2.5.1 ABH Principle of Operation

Consider an inhomogeneous beam under the Euler-Bernoulli assumptions [4]. The free response of the beam in the linear response regime is governed by:

$$B(x)\frac{\partial^4 w(x,t)}{\partial x^4} + \rho\frac{\partial^2 w(x,t)}{\partial t^2} = 0 \tag{7}$$

where $W(x)$ is the flexural displacement, $\rho$ is the mass density, $B(x) = E(x)h(x)^3/12(1-\nu^2)$ is the bending stiffness, $E(x)$ is the Young's modulus, $h(x) = \epsilon x^m$ is the varying thickness, $\nu$ is the poisson's ratio, and $m$ is a real-valued constant that defines the power-law profile.

The geometrical acoustics approximation assumes a propagating wave in a steady state is given by:

$$w(x,t) = We^{kx+i\omega t} \tag{8}$$

where $k$ is the flexural wave number (also $k = \frac{\omega}{c}$), $\omega$ is the angular frequency of the wave, and $c$ is the flexural wave velocity. Substituting Eq. (8) into Eq. (7) gives

$$B(x)k^4We^{kx+i\omega t} - \rho\omega^2We^{kx+i\omega t} = 0 \tag{9}$$

With some rearrangement, the flexural wave number, $k$ can be expressed as:

$$k(x) = \left(\frac{12\rho(1-\nu^2)\omega^2}{Eh(x)^2}\right) \tag{10}$$

Furthermore, the wave velocity wavelength and amplitude of the propagating wave can be expressed as

$$c(x) = \left(\frac{E\omega^2}{12\rho(1-\nu^2)}\right)^{1/4}\sqrt{h(x)} \tag{11}$$

$$\lambda(x) = \left(\frac{4\pi^4 E}{3\rho(1-\nu^2)\omega^2)}\right)^{1/4}\sqrt{h(x)} \tag{12}$$

$$W(x) = W(x_{ABH})\left(\frac{h(x_{ABH})}{h_{uniform}}\right)^{3/4} \tag{13}$$

Eq. 11 shows that the phase velocity of the flexural wave is directly proportional to the thickness of the beam. In the case of an ideal wedge where the thickness vanishes at the end of the wedge, the velocity of incoming flexural waves gradually decreases, ultimately reaching zero. This phenomenon results in a fully trapped, non-reflected wave. Equally, the inverse relationship between the amplitude and beam thickness, as described in Eq. 13, indicates the particle displacement at the wedge tip approaching infinity, essentially creating a point of singularity. This characteristic, resembling the behavior of optical black holes, led Krylov to coin the term "acoustic black holes" in describing these structures [5].

However, in practical applications, achieving a beam with exactly zero thickness is not feasible and there will always be some residual thickness. Studies have shown that even a very thin residual thickness can have a detrimental influence on the reflection properties of the beam [36]. This issue is typically resolved by including a light dissipative layer in the retarding region of the beam. The role of this dissipative layer is to convert the strain energy of the flexural waves into heat, effectively damping the vibrations and reducing the reflection coefficient. Figure 2.7 illustrates the effect of including dissipative layers. The beam without these layers maintains a reflection coefficient above 0.8 across the entire frequency range examined, whereas the beam with dissipative layers experiences a gradual reduction in the reflection coefficient.

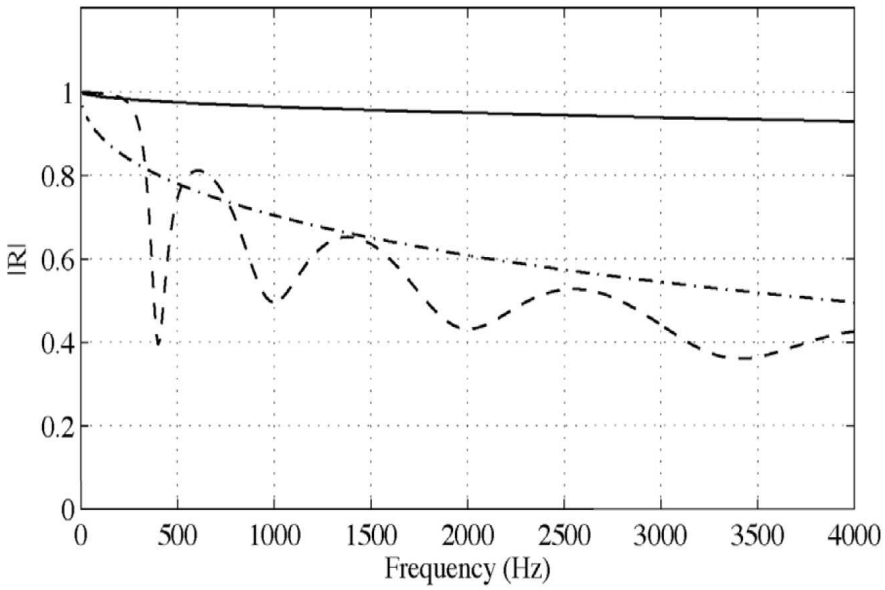


Figure 2.7: Reflection coefficient predicted by the geometrical acoustics model without (solid line) and with (dashed-dotted line) a damping layer, and by plane wave model with damping layer (dashed line) [36]

### 2.5.2 Design and Performance of ABH Beams

#### Reflection Coefficient

The reflection coefficient is a quantity that describes the amount of wave reflected in the beam after reaching the boundaries. Its calculation depends on the numerical approach used to solve the governing equation 4. In Figure 2.7, the monotonic variations in the reflection coefficients over the frequency range without (solid line) and with (dashed-dotted line) damping is derived from geometrical acoustic solution further integrating the complex wave number; see Eq. 14. On the contrary, the plane wave approximation reveals an oscillatory trend in the reflection coefficient, as shown in Figure 2.7. Each minimum in the reflection coefficient corresponds to a resonant mode of the ABH cell (an ABH cell only comprises the retarding region of the ABH beam); see Table 2.1. This explanation aligns with findings of Hook et al. [27], using a wave decomposition approach to obtain the reflection coefficient; see Figure 2.8. Therefore, modeling the ABH unit cell and determining its natural frequency can be a valuable tool for predicting the beam reflection performance, especially when optimizing the reflection coefficient in the design stage over a broad or narrow frequency

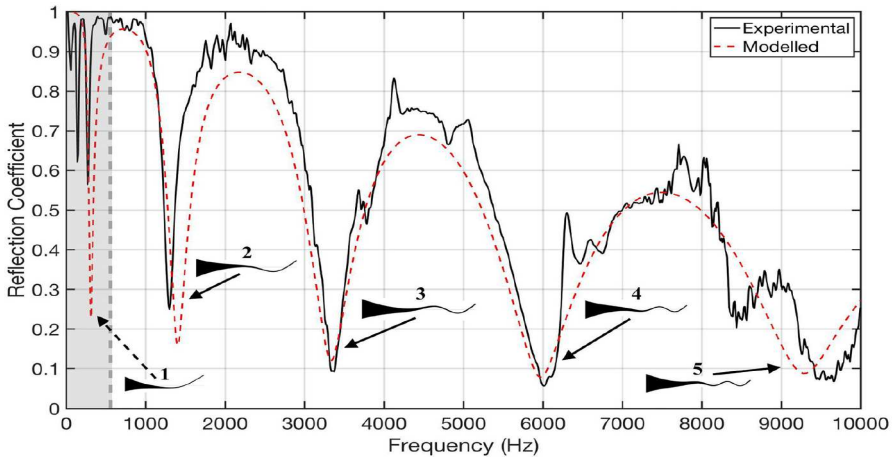


Figure 2.8: Comparison of reflection coefficients using the decomposition method by experiments and Finite Element (FE) model [27]

range.

$$R = \exp\left(-2\int_{x_0}^{x} Im(k(x))\, dx\right) \tag{14}$$

**Cut-on frequency**

The cut-on frequency of an ABH is another parameter that designers can optimize. Below the cut-on frequency, the ABH does not effectively absorb or interact with incoming waves. To enable interaction, the characteristic size of the ABH, such as the length of the retarding region in a beam or the diameter of an axisymmetric taper in an indented plate, must be at least as large as the wavelength of the incoming wave. An approximate analytical expression for the cut-on frequency of a beam is given by [36]:

$$f_{cut-on} = \frac{h_0}{2\pi L_{ABH}^2}\sqrt{\frac{E_0[40-24\nu]}{12\rho(1-\nu^2)}} \tag{15}$$

where $h_0$ is the thickness of the uniform beam outside the ABH region, $L_{ABH}$ is the length of the ABH region and $\nu$ is the poisson's ratio

The relationship between the cut-on frequency and the length of the ABH region, given a uniform thickness, is described by Eq. 15. A parametric study carried out by Aklouche reveals that the

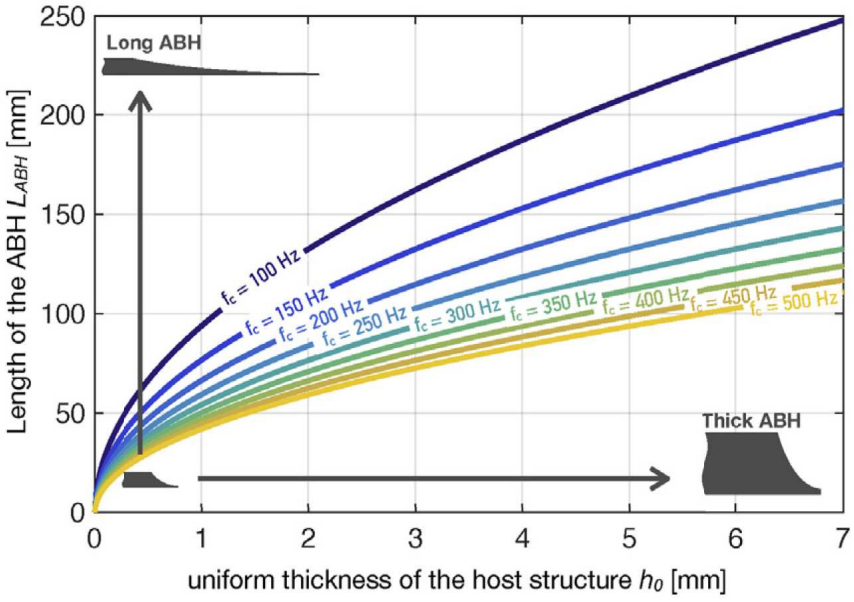


Figure 2.9: Parametric study of cut-on frequency of an ABH beam defined by Eq. 15 [14]

cut-on frequency also depends on the height of the wedge tip [14]. Figure 2.9 illustrates how the cut-on frequency can be improved by maximizing the length of the ABH region and minimizing the height of the wedge tip.

From a structural perspective, concerns have followed regarding the performance of ABH beams or plates under static loads and fatigue analysis. These concerns have motivated design modifications, such as the compound ABH, which has demonstrated improved static strength while preserving the ABH effect [23]. In this work, a compound ABH design is incorporated.

### Smoothness Criterion

A smoothness criterion is also imposed to ensure that the flexural wave number does not vary significantly to avoid producing reflected components along the thickness profile $h(x)$ of the ABH region. It states that the spatial variation of the flexural wave number must be smaller over a distance of the wavelength order [12], [28], mathematically expressed as:

$$\frac{dk}{dx}\frac{1}{k} \ll k \tag{16}$$

This condition is naturally satisfied for power law values $m \geq 2$.

### 2.5.3 ABH in plates

The concept of ABH was initially extended to plates by Krylov [5]. This extension involved embedding axisymmetric circular indentations in plates with a decreasing thickness according to the power law. Ever since, numerous computational and experimental studies have contributed to a deeper understanding of the ABH effect in plates, as a stepping stone towards more practical applications. In general, the response observed in plates aligns with what has been observed in beams. Conlon et al. captures the distributed amplitude of an ABH plate around the cut-on frequency, as shown in Figure 2.10b [12]. It shows that maximum amplitudes are concentrated in the ABH region, which is consistent with the theories discussed in Section 2.5. While these amplitudes are indeed concentrated in the ABH region, the overall vibration levels are reduced compared to a uniform plate. Conlon et al reports that an ABH plate can achieve up to a 20 dB reduction in vibration levels beyond the cut-on frequency [12]; see Figure 2.10c. For a more detailed description of the numerical model and results, the reader is referred to [12].

Studies have delved into various aspects of ABH structures, going beyond the simple observation of physical deflection. For instance, Climente et al. [9] uses a line source to excite Lamb waves in an ABH plate. This excitation method allowed for the visualization of wave trajectories in a way that can be challenging to capture for a point source excitation. The focusing effect can be analysed based on the thin plate formulation under geometrical acoustics assumptions [25]. As shown in Figure 2.11, it is evident that the waves are progressively directed toward the center of the plate, indicating an energy-focusing effect at the ABH center. In essence, the acoustic black hole can be likened to a waveguide. This focusing effect has been explored in various applications of ABH structures, including piezoelectric energy harvesting and optical lens focusing [10].

#### Design and Performance of ABH Plates

Modal analysis is another method used to describe the performance of ABH structures. As mentioned in Section 2.5.2, ABH cell modes can be linked to the reflection coefficient in beams. This observation is supported by Conlon et al. who have shown that the modal loss factor of a plate

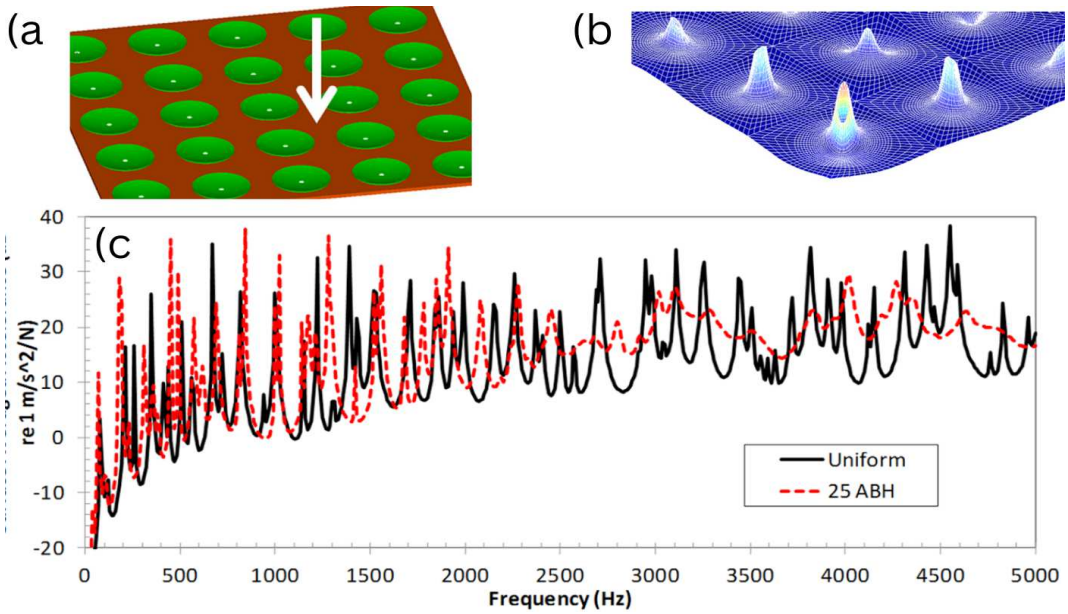


Figure 2.10: (a) Periodic grid layout of ABHs in plate (b) Distributed amplitude of ABH plate around the cut-on frequency (c) Comparison of surface averaged acceleration of uniform plate vs ABH plate [12]

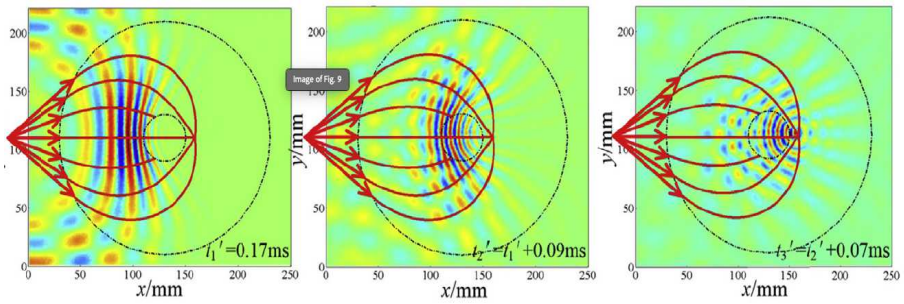


Figure 2.11: time snapshots showing the focusing effects of ABHs on incoming wavefield [25]

indented with multiple ABH can be related to the modal loss factor of an individual ABH cell [12]. Additionally, Hook et al report an exponential increase in modal density as the ABH tip height is decreased and a linear increase in modal density as the ABH length is increased [27]. Finally, Li & Ding highlighted how the mode shape of an ABH beam interacts more effectively with the ABH region when the length of the ABH region is increased [28]. All of these studies contribute to the consensus that maximizing the ABH effect involves increasing the length of the retarding region and reducing the thickness of the wedge tip as much as possible.

### 2.5.4 Design of ABHs in Structures

Implementation of the ABH in structural design can be bounded by constraints. In cases where the length or terminating thickness of the ABH is fixed, the power law can be modified to improve the ABH performance [27]. However, the boundaries of many structural members are not free, which impedes practical realization of the ABHs in structures. This can be resolved through various design proposals such as embedded ABH and surface-mounted ABH.

The embedded ABH consists of multiple indentations along a beam or plate. Research has shown that having more indentations can collectively improve the absorption efficiency [22]. Moreover, larger ABH regions tend to lower the cut-on frequency, which means fewer indentations can be accommodated on a structure. Ultimately, the performance of a multiply indented structure will depend on a cell mode. The designer's choice lies between optimizing the ABH size, number of indentations, and overall stiffness which is compromised by the indentation. Figure 2.12a shows how multiple ABH can be implemented in beams while Figure 2.12b shows how multiple ABH can be implemented in plates

Rather than on the surface, the ABH can also be tunneled within a plate. Figure 2.12c shows a tunneled ABH with and without a stud, correspondingly. A stud can be introduced to improve the strength of the plate while introducing continuities that may be beneficial in the dynamic response [30]. Indeed, a form of this application is implemented in this work, where indentations are embedded between the plies of the CLT; See Section 3 for a detailed description of the numerical model.

The ABH can also be implemented as a secondary structure as in the case of surface-mounted

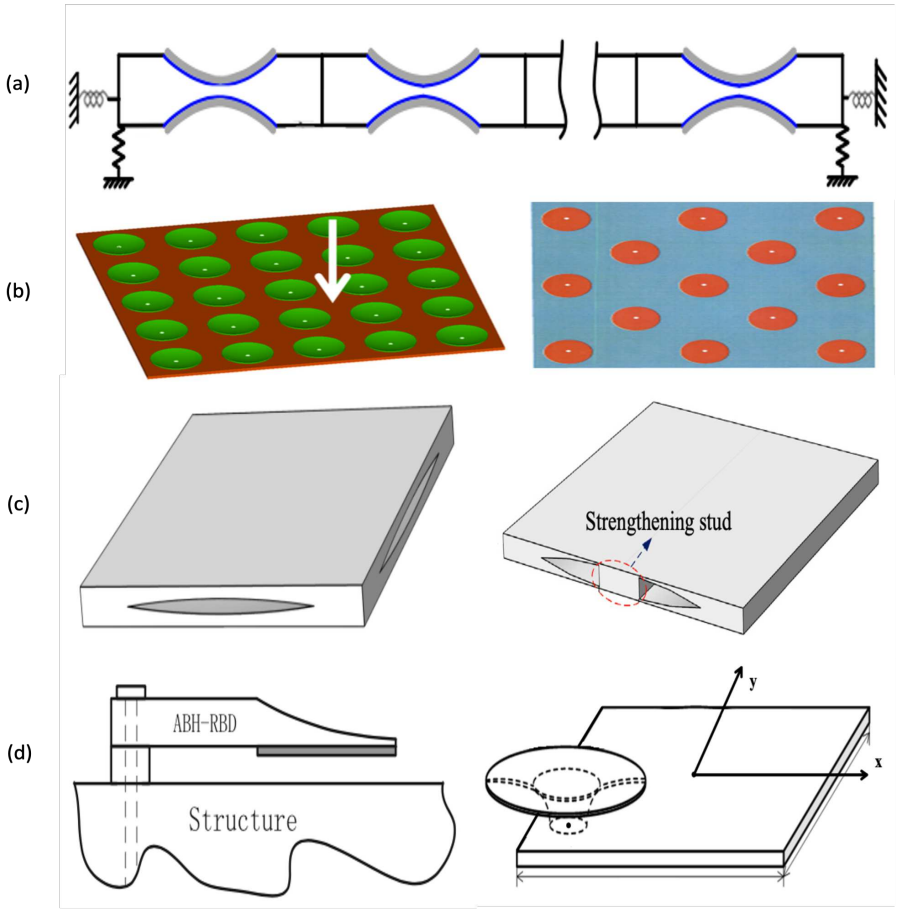


Figure 2.12: Implementation of ABH in structures. Multiple embedded ABH (a) along a beam [22], (b) in a plate [12]. (c) ABH tunnelled into a plate without strengthening studs (left) and with strengthening studs (right) [30]. (d) ABH beam acting as a resonator (left) and ABH plate acting as a resonator (right) [37].

ABH. These are generally designed as resonators; therefore, the ABH must be carefully placed to couple effectively with the primary structure. Figure 2.12d shows how the ABH acts as a resonant damper for a beam and plate. Placement of the resonators takes into consideration the structural response of the primary structure, its boundary conditions, and many more factors.

## 2.6 Numerical Modelling of ABH Structures

In addition to the analytical procedures discussed for evaluating the response of an inhomogeneous beam, the finite element method has also been employed in the study of acoustic black hole (ABH) beams. This numerical method discretizes the governing equation, Eq. 4 over the domain, allowing it to be implemented in a standard finite element code. Interestingly, the transfer matrix method, generally considered analytical [28], [36], also discretizes the domain but has not kept up with advances in the finite element method.

Hook et al. conducted a parametric study of ABH terminations in a beam using Timoshenko beam elements in COMSOL and validated a specific ABH beam configuration experimentally [27]. Note that the use of beam elements in finite element modeling leads to ABH tapers that are symmetric about the beam axis, as illustrated in Figure 2.13. This may not align with many pictorial representations of ABH beams in the literature, for example, see Figure 2.6. However, this approach aligns with the formulation of the beam equation which is done about the neutral axis. It remains unclear why the beam formulation agrees with experimental models, especially when the beam is not symmetrically cut about its neutral axis. Additionally, it is uncertain under what geometrical size and conditions this model ceases to agree with experimental results. These areas present potential avenues for future investigations.

In the absence of an experimental setup, element verification tests can be used to assess the consistency of numerical results. The FE model developed in [27] can be checked against 2D elements by comparing the natural frequencies of an ABH cell that is symmetrically cut ($ABH_{2D,1}$) and another that is cut on one side ($ABH_{2D,2}$), to reflect the cell modes reported by hook, a fixed boundary condition is applied at the end. Table 2.1 displays the first four modes of vibration for the three configurations; Firstly, notice that the first four natural frequencies corresponds to the dips

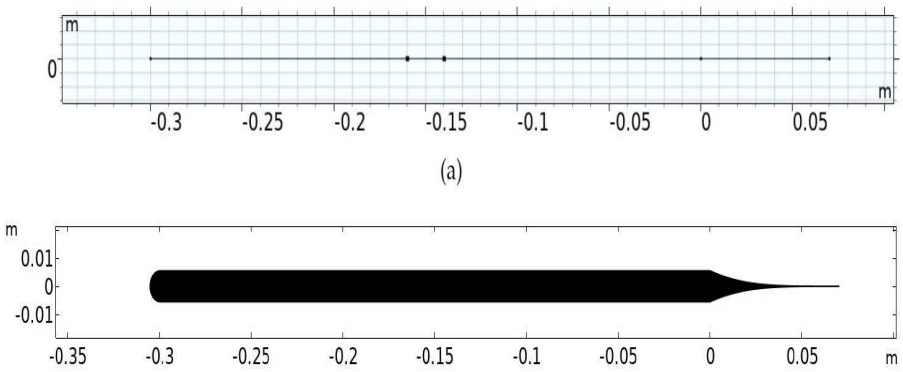


Figure 2.13: ABH beam modelled using Timoshenko beam elements (above) and the corresponding 2D representation (below) [27].

in reflection coefficient observed in Figure 2.8, this implies that the mode shapes create a standing wave pattern preventing the propagation of transverse waves in the beam. However, while the natural frequencies of the 2D elements agree with each other, they disagree with the beam element; with a 30% error relative to the beam across all modes. Therefore, when modelling an ABH plate, there is a lingering concern about the relative error of solid elements to shell elements.

Table 2.1: Comparison of Natural frequencies of an ABH cell modelled using Beam elements and 2D elements

| Natural Frequencies | Beam Elements (Hz) | $ABH_{2D,1}$ (Hz) | $ABH_{2D,2}$ (Hz) |
|---|---|---|---|
| 1 | 388.65 | 511.75 | 511.26 |
| 2 | 1628.1 | 2128.0 | 2119.0 |
| 3 | 3582.7 | 4662.7 | 4619.5 |
| 4 | 6140.2 | 7981.9 | 7898.4 |

However, using solid elements to model plates offers greater flexibility, especially when dealing with complex geometries like multiple ABH indentations. In this project, solid elements are chosen for modeling the CLT panels with ABH due to their flexibility, and because they can capture the through-thickness mode contributions from each composite layer.

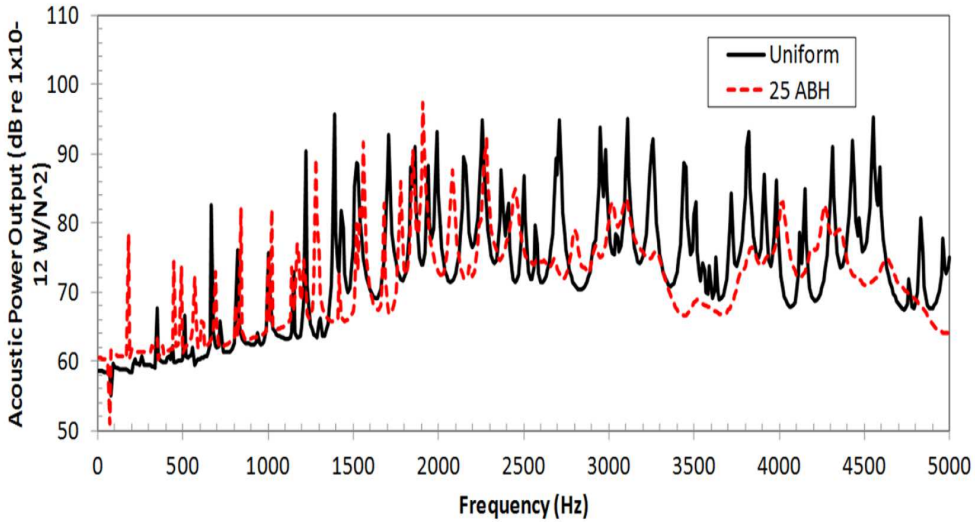


Figure 2.14: Comparison of radiated sound power of Uniform plate vs ABH plate [12]

## 2.7 Acoustic Black Hole Effect in Low Frequency Noise Reduction

Impact noise is generated when a vibrating structure interacts with air, Section 2.2.1 discusses this topic in detail. CLT floors, due to their low mass and high stiffness, typically exhibit poor acoustic properties, particularly in the low frequency range. This project proposes the implementation of embedded ABH to mitigate low-frequency impact noise. In practical applications, ABH can be integrated with existing noise insulation technologies discussed in Section 2.3.1.

Extensive research has been conducted to study the reduction in sound radiation achieved by incorporating acoustic black holes into structures. It is not surprising that beams or plates with acoustic black holes can reduce radiated sound because the acoustic pressure at the surface is strongly coupled with the mobility at the structure's surface. In Figure 2.14, comparison of the resulting acoustic power radiated from the uniform plate and an ABH plate illustrates that the two plates exhibit similar acoustic trends until the cut-on frequency near 2500 Hz where the ABH shows reduction in acoustic power up to 20 dB [12]. Therefore, the cut-on frequency, originally defined in terms of the bending waves of the plate in Section 2.5.2, can indirectly capture the acoustic performance of structures with ABH.

## 2.8 Overview of the FE Formulation for Fluid-Structure Analysis

Only the formulation for the steady-state procedure will be summarized as it pertains to the methodology used in this project. The reader is referred to [16] for more details on vibro-acoustic analysis using the FEM. The formulation begins with the definition of the equilibrium equations for small-amplitude motion of a compressible, adiabatic fluid.

$$\frac{\partial p}{\partial \mathbf{X}} + \gamma \dot{\mathbf{U}} + \rho \ddot{\mathbf{U}} = 0 \tag{17}$$

where $\ddot{\mathbf{U}}$ is the fluid particle acceleration vector, $\dot{\mathbf{U}}$ is the fluid particle velocity vector, $p$ is the pressure in excess of static pressure, and $\mathbf{X}(x, y, z)$ is the spatial position of the fluid particle, $\gamma$ is the volumetric drag and $\rho$ is the fluid density. In addition, the constitutive behavior of an inviscid, linear, compressible fluid is expressed as

$$p = -k \frac{\partial}{\partial \mathbf{X}} \tag{18}$$

where $k$ is the bulk modulus of the fluid. If the solutions are assumed to vary harmonically

$$\mathbf{U} = \overline{\mathbf{U}} e^{i\omega t}$$

$$\mathbf{p} = \overline{\mathbf{p}} e^{i\omega t}$$

Equ 17 can be rewritten in terms of its assumed solution

$$\frac{\partial \overline{\mathbf{p}}}{\partial \mathbf{X}} - \omega^2 \overline{\rho} \overline{\mathbf{U}} = 0 \tag{19}$$

where $\overline{\rho} = \rho + \frac{\gamma}{i\omega}$ is defined as the complex density. Furthermore, differentiate Equ 19 with respect to $\mathbf{X}$, divide by $\overline{\rho}$ and substitute Equ 18 and its derivatives to obtain the equilibrium in terms of pressure

$$-\omega^2 \frac{1}{k} \overline{\mathbf{p}} - \frac{\partial}{\partial \mathbf{X}} \left( \frac{1}{\overline{\rho}} \frac{\partial \overline{\mathbf{p}}}{\partial \mathbf{X}} \right) = 0 \tag{20}$$

Eq. 20 is transformed into its weak form by introducing the variational statement over the volume of the fluid

$$\int_V \delta\mathbf{p}\left[-\omega^2\frac{1}{k}\overline{\mathbf{p}} - \frac{\partial}{\partial\mathbf{X}}\left(\frac{1}{\overline{\rho}}\frac{\partial\overline{\mathbf{p}}}{\partial\mathbf{X}}\right)\right]dV = 0 \tag{21}$$

Integrating by parts and applying Green's theorem results in

$$-\int_V \delta\mathbf{p}\frac{\omega^2}{k}\overline{\mathbf{p}}dV + \int_V \frac{1}{\overline{\rho}}\frac{\partial\delta p}{\partial\mathbf{X}}\frac{\partial\overline{\mathbf{p}}}{\partial\mathbf{X}}dV + \int_S \delta p\frac{1}{\overline{\rho}}\frac{\partial\overline{\mathbf{p}}}{\partial\mathbf{X}}\mathbf{n}^- dS = 0 \tag{22}$$

the volume integrals satisfy equilibrium and the surface integrals describe the boundary traction. In the absence of an intervening layer such as a rug or foam, the solid and fluid are in perfect contact, and their displacements are tied [16]. This assumption can be written as [7]

$$\mathbf{n}^-\overline{\mathbf{U}} = \mathbf{n}^-\overline{\mathbf{U}}_m$$

where $\overline{\mathbf{U}}_m$ is the solid displacement. Equ 19 then becomes

$$\frac{1}{\overline{\rho}}\frac{\partial\overline{\mathbf{p}}}{\partial\mathbf{X}} = -\omega^2\mathbf{n}^-\overline{\mathbf{U}}_m$$

Therefore, the final variational statement is

$$-\int_V \delta\mathbf{p}\frac{\omega^2}{k}\overline{\mathbf{p}}dV + \int_V \frac{1}{\overline{\rho}}\frac{\partial\delta p}{\partial\mathbf{X}}\frac{\partial\overline{\mathbf{p}}}{\partial\mathbf{X}}dV + \int_S \delta p\left(-\omega^2\mathbf{n}^-\overline{\mathbf{U}}_m\right)dS = 0 \tag{23}$$

To complete the structural-acoustic formulation, the structural response $\overline{\mathbf{U}}_m$ is governed by a similar variational statement of the virtual work

$$\int_V \delta\varepsilon(\omega) : \sigma(\omega)dV + \int_V \dot{\mathbf{U}}_m(\omega)dV + \int_V \rho\delta\mathbf{U}_m(\omega)\ddot{\mathbf{U}}_m(\omega)dV + \int_{S_{fs}} p\delta\mathbf{U}_m(\omega)\mathbf{n}^- dS_{fs} - \int_{S_t}\delta\mathbf{U}_m(\omega)\mathbf{t}dS_t = 0 \tag{24}$$

where the volume integrals satisfy equilibrium, the surface integral $\int_{S_{fs}}$ describes the influence of

the acoustic medium on the structure (this influence is very small because the structural response dominates the system), and the surface integral $\int_{S_t}$ describes the traction boundary on the solid. $\mathbf{t}$ is the surface traction and the strain field $\delta\varepsilon_m$ is compatible with the displacement field $\delta\mathbf{U}_m$.

### 2.8.1 Discretizing the Variational Field

The variational statements Equ 23 and 24 are discretized by introducing interpolation functions $p = \boldsymbol{H^P}\mathbf{p}^{\boldsymbol{P}}, \boldsymbol{P} = 1, 2, 3, ...$ for all the pressure degrees of freedom, and $\mathbf{U}_m = \boldsymbol{N^N}\mathbf{u}^{\boldsymbol{N}}, \boldsymbol{N} = 1, 2, 3, ...$ for all the displacement degrees of freedom. The resulting equation is inverted to solve for pressures and displacements

$$\left[\mathbf{K} - i\omega\mathbf{C} - \omega^2\mathbf{M}\right]\mathbf{A} = \mathbf{F}$$

where $\mathbf{K}$ is the coupled stiffness matrix, $\mathbf{C}$ is the coupled damping matrix (although this term only contains damping contributions from the structure as the volumetric drag in the fluid are negligible), $\mathbf{M}$ is the coupled mass matrix, $\mathbf{F}$ is the traction from the solid medium and $\mathbf{A}$ is a vector of all pressure and displacement degrees of freedom.

### 2.8.2 Addressing Acoustic Exterior Problems

The need may arise to study acoustic exterior problems such as a vibrating structure in a fluid medium of infinite extent. In a more general term, such studies try to eliminate the influence of reflected waves on the region of interest. For example, while a CLT floor is not realistically placed in an infinite domain, reflected sound waves from walls and ceiling would introduce disturbances in the pressure output readings. More so, those reflected components would depend on the size of the room.

Exterior problems can be addressed in FEM by defining a radiating (non-reflecting impedance) boundary condition on the traction surface [11], [16]. Consider the variational statement in Equ 22, previously the solid fluid coupling was defined on the boundary traction, but the radiation boundary can also be included. Let the surface be called $S_{rad}$:

$$\int_{S_{rad}} \delta p \frac{1}{\overline{\rho}} \frac{\partial \overline{\mathbf{p}}}{\partial \mathbf{X}} \mathbf{n}^{-} dS$$

the surface traction for an impedance boundary describes an imposed impedance or admittance by a layer of material on the fluid. It is modelled as spring and dashpot in series, distributed between the acoustic medium and a rigid wall

$$\frac{1}{\overline{\rho}} \frac{\partial \overline{\mathbf{p}}}{\partial \mathbf{X}} = -\left( \frac{i\omega}{c_1} - \frac{\omega^2}{k_1} \right) \overline{\mathbf{p}}$$

however, in a radiating boundary these admittance values are mapped to the geometry of the radiating surface using a Dirichelet-to-Neumann map [11], [16]. The reader is referred to [11], [16] for detailed procedure of the mapping as well as sample admittance values for plane, circular and spherical boundaries.

Another approach to modelling exterior problems in FEM involves the use of infinite acoustic elements. Just like finite elements they have basis functions which are however formulated to satisfy radiation conditions by mapping the element to an infinite domain. Infinite acoustic elements can be defined directly on the terminating surface of the finite element mesh but unlike impedance boundary they do not cause traction forces on the surface boundaries.

Perfectly matched layers can be equally employed in place of radiating boundaries or infinite acoustic elements. They are acoustic finite elements with behaviours modified appropriately to act as absorbing layers. They are attached directly to the bounded fluid domain just like infinite elements, however, being a finite element introduces a new surface boundary. To complete the formulation, zero pressure boundary conditions are exacted on the surface boundary which is another key element that distinguishes them from finite elements in the bounded domain; their surface boundaries cannot couple with the solid medium.

When modelling acoustic exterior problems, these various modelling practices that help to capture the unbounded domain can by verified against each other to establish confidence in results. Usually, their formulations are robust enough and do not to cause significant differences. Eventually, the most computationally efficient domain can be chosen for further investigation

## 2.9 Summary

This chapter presented the state of the art in CLT and ABH in a topical manner and discussed the potential for combining the two technologies to achieve low-frequency vibration and noise reduction, an elusive problem in wooden building construction. The effectiveness of ABH structures in achieving low-frequency impact noise reduction in CLT is not established yet.

To provide a solution for this problem, the objective is to achieve an *ABH effect* in the frequency range of 50-800 Hz. The effectiveness of the solution can be quantified by its cut-on frequency and its reduction in the magnitude of structural and acoustic response in the specified range. The cut-on frequency of an ABH can be decreased by increasing the length of the retarding region or reducing the thickness of the wedge tip. Therefore, it is possible to enhance the cut-on frequency of ABH structures by increasing the length of the ABH region from 9 cm [12], [28] to higher values. For example, Li & Ding observed a decrease in the cut-on frequency, from the third resonance at 453 Hz to the second resonance at 160 Hz when the length of the ABH region is increased from 9 cm to 15 cm [28].

It is important to recognize that a large number of ABH studies have focused on metals such as aluminum or steel with low hysteresis damping, for example, structural damping ratios ranging from 0.0001 [27] to 0.001 [12]. Wood has higher energy dissipation, with structural damping ratio as high as 0.1 [38]. Since the damping in the ABH region can be further increased, it follows that the overall damping of the structure can be improved. The ABH region can be seen as a pocket of space provided to include material dampers to raise the aggregate damping of the structure.

This project investigates the reduction of low-frequency impact noise in a CLT floor with multiple ABH indentations. The following chapter provides a detailed description of the model used in this study. A parametric study is employed to uncover trends related to the cut-on frequency and its correlation with impact sound radiation from the floor.

# Chapter 3

# Methodology

The motivation to choose Cross Laminated Timber (CLT) as a construction material in residential and commercial buildings has been extensively addressed in chapter 2. Acoustic Black Holes (ABH) have been shown to attenuate vibration and consequently sound radiation in structures, mathematically speaking, due to the coupled fluid-structure interface, see Eq. 23. Various designs to integrate ABH in structures have been proposed primarily due to boundary constraints and concerns stemming from static structural integrity and fatigue; see Section 2.5.4. Indeed, some configurations may also optimize dynamic responses such as reflection coefficient, transfer mobility, and sound radiation. However, many propositions in the literature have generally focused on metals. This work extends the existing literature by integrating ABH in CLT to investigate the vibro-acoustic response and determine whether there is an improvement in acoustic response when compared to a CLT without ABH. Specifically, this project highlights a prominent drawback in using CLT as a building construction material: its capacity to attenuate low frequency impact noise.

The literature has shown that ABH performance can be modified by altering geometrical properties such as taper length, tip height, and power law [27]. In the case of axisymmetric profile indentations on a plate, the outer radius is used in place of taper length. Therefore, either optimization or parametric study can be used to check the possibility of achieving the *ABH effects* in the low-frequency region. In this work, a parametric study is carried out to provide a more detailed insight into the intricate effects that each parameter has on the vibro-acoustic response in the low-frequency range, ultimately informing decisions on optimizing geometrical parameters within

practical constraints. The finite element method is used for this study because it can be easily adapted to a variety of configurations to solve a variety of configurations easily; a summary of the finite element procedure for a vibro-acoustic model is summarized in Section 2.8.

The numerical model consists of a 3-ply CLT floor in a half-baffled acoustic medium. The flexural waves are then analyzed to obtain the surface-averaged acceleration of the plate and sound radiation in the acoustic medium. The results highlight trends in the performance of the ABH measured in terms of the cut-on frequency and band level attenuation of the acoustic response when compared with a CLT floor without ABH indentations.

In this chapter, the geometrical and physical properties of the model are presented, followed by a discussion of the finite element modeling procedure, highlighting key components such as the boundary and traction conditions, discretization of the medium and convergence analyses. This part explains the post-processing method to obtain the radiated sound power, which sets the foundation for the acoustic response presented in the chapter 4.

## 3.1 Model description

The FE model has been implemented in Abaqus Standard [16]. A 3D model is chosen for the parametric study because it allows more flexibility in defining geometrical properties compared to a 2D model. Indeed, 2D models that utilize shell elements can also be used to define ABH indentations; however, this procedure is not commonly used in the literature because it requires cumbersome implementations that involve varying section properties [39]. More over shell elements to not accurately account for contributions from thickness modes at increasing frequencies, see Section 2.4.

Figure 3.1 highlights the geometry of the floor, the height of each ply, lay-up sequence, and periodic indentation of the ABHs. Figure 3.2 shows the geometric profile of each ABH indentation that is etched out in each ply. Only the geometrical properties of the ABH profile and the number of indentations are considered for the parametric study. This is because the number of indentations introduces a limiting factor in the maximum size of the achievable radii values. Table 3.1 shows the range of parameters considered in this study. The height function of each ABH indentation is

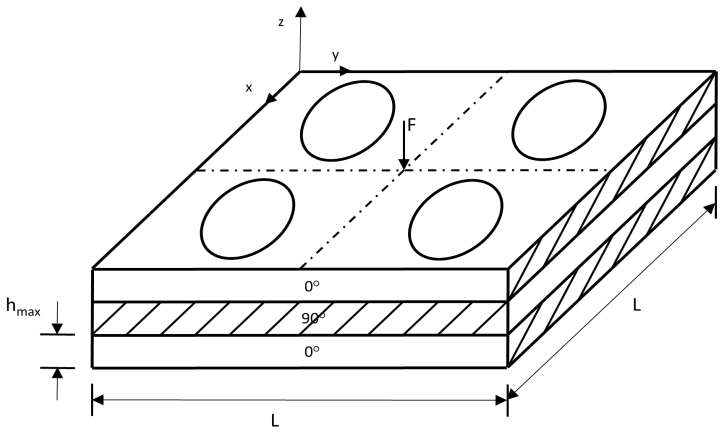


Figure 3.1: Geometric properties of 3 ply CLT floor indicating the length $L$, height of each ply $h_{max}$, and layup sequence $0°/90°/0°$

defined as

$$h(x) = [h_{max} - h_{min}] \left( \frac{x}{R - r} \right)^{\mu} + h_{min}$$

Table 3.1: Geometric properties of 1 ply CLT with ABH indentations

| Varying Properties | | Fixed properties | |
|---|---|---|---|
| No of indentations | Range of outer radius, R | Parameter | Value |
| 25 | 100 - 150 mm | $h_{max}$ | 35 mm |
| 16 | 100 - 200 mm | $h_{min}$ | 10 mm |
| 9 | 100 - 250 mm | $L$ | 2 m |
| 4 | 100 - 450 mm | $L$ | 2 m |
| | | r | 30 mm |
| | | $\mu$ | 2.5 |
| | | $F$ | 1 N |

In addition to the geometrical properties, Table 3.2 describes the material properties of the CLT floor, where the subscripts ABH denote material properties in the ABH region for the floor. The material properties obtained from the literature [38]. A separate structural damping value, $\eta_{ABH}$ of 0.03 is applied in the ABH region to reflect the additional damping introduced by a dissipating layer placed in the region. An additional non-structural mass of 18 g is evenly distributed in the ABH

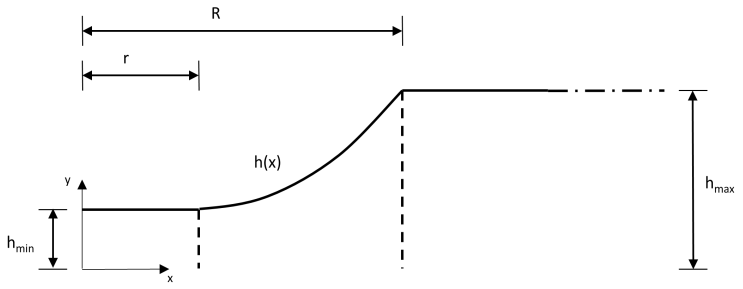


Figure 3.2: ABH profile highlighting the geometrical features of each indentation in a ply

region. The additional mass is conservatively chosen to avoid the mass law effect. It is important to note that the non-structural mass does not contribute to the stiffness matrix in the finite element mathematical procedure. The boundary conditions of the plate are all set to free and a harmonic excitation of amplitude 1 N is applied at the centre of the floor. In the case of an odd number of indentations, the force is offset 0.2m from the floor centre for the 25-ABH and offset 0.66m from the floor centre for the 9-ABH, this is done in order to apply the force at the uniform region.

Table 3.2: Material Properties and stacking sequence [38]

| Property | Value |
|---|---|
| $E_x$ | $1.1 \times 10^{10} \quad Nm^{-2}$ |
| $E_y$ | $3.67 \times 10^{8} \quad Nm^{-2}$ |
| $E_z$ | $3.67 \times 10^{8} \quad Nm^{-2}$ |
| $G_{xy}$ | $6.9 \times 10^{8} \quad Nm^{-2}$ |
| $G_{yz}$ | $6.9 \times 10^{7} \quad Nm^{-2}$ |
| $G_{xz}$ | $6.9 \times 10^{8} \quad Nm^{-2}$ |
| $\nu_{yx}$ | 0.014 |
| $\nu_{xy}$ | 0.030 |
| $\nu_{xz}$ | 0.014 |
| $\rho$ | $450 \quad kgm^{-3}$ |
| $\eta$ | 0.02 |
| $\eta_{abh}$ | 0.03 |
| Layup sequence | $0°/90°/0°$ |

Four floor configurations are considered in this parametric study, shown in Figure 3.3: (a) a CLT floor with 5 x 5 periodically spaced grid of embedded ABH (b) a CLT floor with 4 x 4 periodically spaced grid of embedded ABH features (c) a CLT floor with 3 x 3 periodically spaced grid of embedded ABH features (d) a CLT floor with 2 x 2 periodically spaced grid if embedded ABH

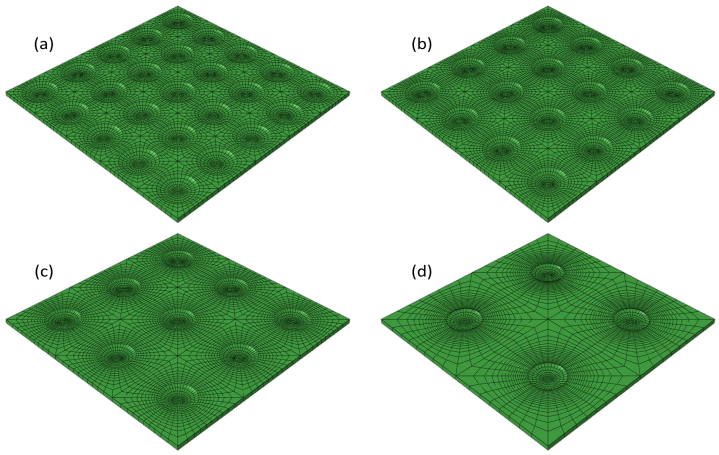


Figure 3.3: ABH grid in one ply of CLT floor. (a) 25 grid, (b) 16 grid, (c) 9 grid and (d) 4 grid

features. A CLT floor without ABH indentations is also constructed for baseline comparison. Unlike the CLT floor with ABH indentations, there is no additional damping applied to specific locations, therefore the floor only contains the baseline structural damping, $\eta = 0.02$.

For the acoustic coupling, the CLT floor is treated as baffled and radiating into half space, thereby mimicking an exterior sound radiation problem. Modeling the traction boundary for exterior acoustic problems can be achieved in a variety of ways, for example using perfectly matched layers (PML), infinite acoustic elements, or non-reflecting impedance boundaries; an extended discussion of these concepts can be found in section 2.8.2. The acoustic medium is modeled as a box spanning 2.2m x 2.2m x 0.025m with impedance boundary conditions applied to the sides and infinite acoustic elements applied to the bottom face. Fluid-structure coupling is achieved through out-of-the-box tie constraints available in Abaqus standard. The bottom surface of the acoustic box is tied to the top surface of the plate, Figure 3.4 shows the interaction setup between the structural and acoustic medium.

Other acoustic models were used to validate the accuracy of the chosen acoustic model, this was done by checking the sensitivity in average sound radiated power at the fluid surface where the tie constraints are applied. For example, the sensitivity was checked against an acoustic model with PML and an acoustic medium with a non-reflecting radiation boundary. The size of the fluid domain was varied to investigate the influence of far-field radiation boundaries on the output response at the

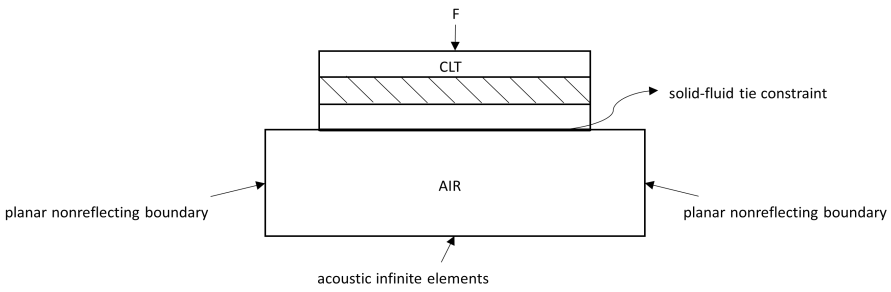


Figure 3.4: Structure-fluid coupling highlighting the CLT floor in a half baffle

interface; section 3.2.2 provides a detailed explanation on the meshing of the acoustic medium. The selection of the chosen acoustic model was primarily in favor of computational requirements. Ideally, the optimal acoustic model for this parametric study has the smallest domain with the least amount of elements both in the structural and acoustic medium. The following section describes the discretization of the structural and acoustic mediums

## 3.2 Discretization and Sensitivity Analysis

It is important to note that the objective of this parametric study is to capture the ABH effect at low frequency. Because the parametric study utilizes a 3D model, the discretization requirements are somewhat relaxed in favor of the time required to perform a round of simulation. With the chosen structural-fluid mesh, each round of simulation takes approximately one hour to complete on a 32-core computer.

### 3.2.1 Meshing of the Structural Medium

The floor configurations are modeled using quadratic brick elements. A minimum of 6 finite elements per wavelength for the maximum targeted frequency is recommended when constructing a numerical model, but 10 elements and more were enforced for conservative purposes. An additional constraint that accounts for the variation in height at the ABH region can be done by setting the reference maximum frequency and corresponding wavelength from the tip where the wavelength is shortest. The bending wave speed for a Kirchoff plate can be written as [12],

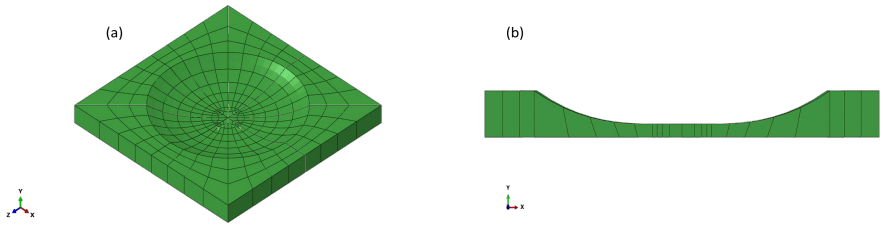


Figure 3.5: Structural mesh of one ABH cell (a) isometric view (b) sectional view

$$c_b(x) = \left( \frac{Eh^2(x)\omega^2}{12\rho(1-\nu^2)} \right)^{1/4} \tag{25}$$

The reference bending wavelength $\lambda = \frac{c_b}{f}$ is taken at the tip of the ABH by replacing $h(x)$ with $h_{min}$.

$$\lambda = \left( \frac{E\omega^2}{12\rho(1-\nu^2)} \right)^{1/4} \frac{\sqrt{h_{min}}}{f} \tag{26}$$

The assumption is further complicated by orthotropic properties of CLT. In Eq. 26, $E = E_z$ and $\nu = \nu_{zx}$, it does not make much difference if $\nu_{zy}$ is chosen because the strains are very small and $\nu$ is squared.

The maximum targeted frequency for the parametric study is 800 Hz. Thus, a 10 element per wavelength requirement will give an element internodal size of 63 mm in the retarding region of the ABH profile. However, in order to capture the gradient in the ABH region more accurately, 2 elements were chosen to discretize the inner radius $r$ which results to an element internodal length of 15 mm. Figure 3.5 shows how the ABH region in one cell is meshed. In the uniform region of the cell ($h(x) = h_{max}$), the discretization requirements are even more relaxed, resulting in an element inter-nodal size of 117 mm.

To guarantee that the meshing procedure was sufficient for a full parameter sweep, a mesh convergence study is conducted starting using the surface-averaged acceleration as the target. Convergence is only checked for CLT floor with 4 x 4 grid ABH indentations with the largest outer radius $R$ of 450 mm. Starting with an element internodal length of 15 mm, Table 3.3 shows that a maximum relative error of 0.4% is introduced as the internodal length is further refined to 5 mm.

This error is accommodated considering the computational resources.

Table 3.3: Convergence: structural medium

| Internodal length in ABH region (m) | Internodal Length in Uniform region | Surface Averaged Acceleration @ 800 Hz (dB re $1 \times 10^{-3} \quad ms^{-2}$) |
|---|---|---|
| 0.015 | 0.030 | 22.597 |
| 0.010 | 0.025 | 22.698 |
| 0.005 | 0.010 | 22.698 |

### 3.2.2 Meshing of Acoustic Medium

The acoustic medium is modeled using quadratic brick elements with acoustic infinite elements applied to the bottom of the acoustic medium. In addition to the impedance-type radiation boundaries, Abaqus also provides acoustic infinite elements for modeling exterior problems. In general, they are defined on the terminating surface of a region of acoustic finite elements and can help reduce the size of the acoustic domain required to accurately model an acoustic medium; see Section 2.8.2 for an extended discussion on modelling exterior problems.

The same requirements of 6 elements per wavelength apply when constructing acoustic elements with a target frequency corresponding to the shortest wavelength. In this study, 10 elements per wavelength have been enforced for conservative purposes. The wavelength of sound can be written as

$$\lambda_f = \frac{c_f}{f} \tag{27}$$

where $c = \sqrt{\frac{K_f}{\rho_f}}$ is the speed of sound, $K_f$ is the bulk modulus and $\rho_f$ is the fluid density. At room conditions, $c \approx 343 m/s$, the required element internodal size $L_{max}$ at 800 Hz is 43 mm.

The acoustic analysis also depends on the far-field properties of the radiation boundary. The radiation boundary conditions converge in the limit as they become infinitely distant from the source. While greater distances between the acoustic source and radiating boundary improve the accuracy of the solution, the computation time increases in proportion with the number of elements. The required standoff thickness between the structure and the radiating boundary can be expressed as [16]

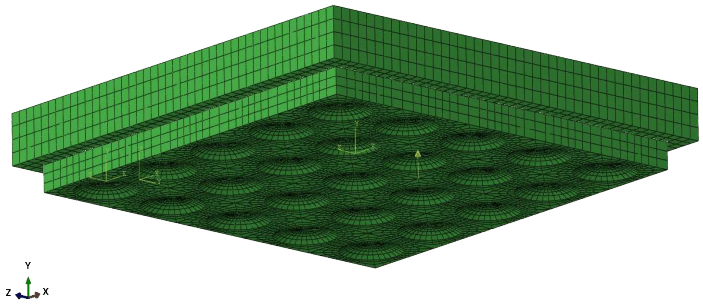

Figure 3.6: Complete FE model for 25-ABH

$$r = \frac{c_f m}{f_m} \tag{28}$$

where $m$ is the number of wavelengths and $f_m$, describes the minimum frequency, i.e. the largest wavelength expected. At room conditions, the required stand-off thickness at 50 Hz and $m = 1/3$ is 2.3 m.

These requirements ensure accurate prediction of all points in the acoustic field and are computationally cumbersome for the parametric study. The requirement in this study is relaxed to predict the acoustic field only at the structural-acoustic interface. Using this criterion, the number of acoustic elements can be reduced as much as possible. Therefore, two convergence studies are used to (1) select the desired number of elements and (2) select the stand-off thickness. Table 3.4 shows that the least amount of elements which consists of an internodal length of 50 mm and a standoff thickness of 200 mm is within 0.3% error of the largest mesh with an internodal length of 25 mm and a stand off thickness of 2 m.

All the configurations in Table 3.4 can be regarded as acceptable because their outcomes are all within 1 dB (this is generally regarded as threshold of audibility for power). However, the least amount of elements was chosen to reduce the computation requirements. Figure 3.6 shows an FE model of the structural and acoustic mesh for the 5 x 5 grid configuration, the same setup is applied for various configurations.

Table 3.4: Convergence: Acoustic medium

| Internodal length (m) | Standoff thickness (m) | Surface Averaged Acoustic Power @ 800 Hz (dB re $1 \times 10^{-12} \quad Wm^{-2}$) |
|---|---|---|
| 0.05 | 2 | 32.4851 |
| 0.04 | 2 | 32.5168 |
| 0.025 | 2 | 32.5870 |
| 0.05 | 0.2 | 32.4951 |
| 0.04 | 0.2 | 32.5266 |
| 0.025 | 0.2 | 32.5960 |

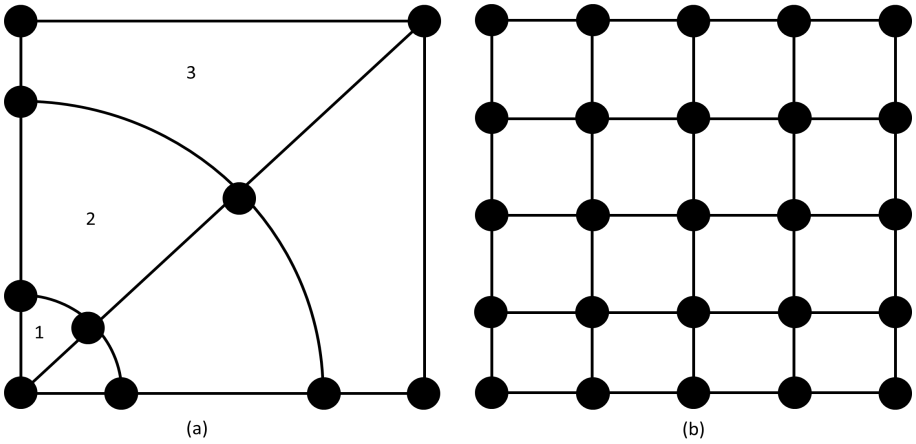


Figure 3.7: Discretization of 1/4 ABH cell using (a) swept mesh and (b) uniform square mesh

### 3.2.3 Obtaining Acoustic Power

Eq. 4 defines the continuous model of radiated sound power in a plate. When the domain is discretized, it becomes difficult to determine an elemental area $dS$ to compute $\Re[pv^*]$ for an arbitrary element shape. For example, consider Figure 3.7 which is a more simplified discretization of 1/4 ABH cell. The surface in Figure 3.7a is meshed with triangles and quadilaterals; and quadratic elements 2 and 3 do not have the same areas. In this case, the nodes would need to be tracked to determine the corresponding areas of elements 1, 2 and 3. However, obtaining the areas of the surface in Figure 3.7b with square meshes is more straightforward, since one element area is known. For this reason, an acoustic mesh similar to the Figure 3.7b was applied.

Many commercial FE codes provide the acoustic intensity as out of the box output quantity,

while some go further to extract the acoustic power over a selected surface using procedures to calculate areas of the elements. In this work, the acoustic power is manually computed from the acoustic intensity output in Abaqus; therefore, it was more convenient to mesh the acoustic medium with equal squares. Although the structural and acoustic meshes do not match geometrically, the Abaqus tie constraint is robust enough to couple the domains suitably.

Additional element verification was carried out to verify the robustness of the Tie Constraint. Specifically, the acoustic surface was meshed like the plate, and compared with an acoustic surface meshed using uniform squares. Both elements reported the same surface averaged intensity within the frequency range under study.

The acoustic intensity vector describes the rate of energy flow in an element obtained at the integration points of the element [16]

$$\bar{\mathbf{I}} = \frac{1}{2}\mathbf{p}\overline{\mathbf{V}}^{*} \tag{29}$$

where $\overline{\mathbf{V}}^{*} = \frac{i}{\bar{\rho}\omega}\frac{\partial\overline{\mathbf{p}}}{\partial\mathbf{X}}$. The acoustic intensity $\bar{\mathbf{I}}$ can be simplified

$$\bar{\mathbf{I}} = \frac{-1}{2i\bar{\rho}^{*}\omega}\overline{\mathbf{p}}\frac{\partial\overline{\mathbf{p}}}{\partial\mathbf{X}}$$

Therefore, the acoustic power can be obtained by adding the real part of intensity (active intensity) on the surface of the fluid panel:

$$\sum_{i=1}^{i=n}\Re[\bar{\mathbf{I}}]\mathbf{S}_i \tag{30}$$

Here, $\mathbf{S}_i$ is the interacting surface area of each element. Eq. 30 shows that if the acoustic mesh consists of uniform elements, at least at the plate-fluid boundary, then obtaining $\mathbf{S}_i$ is straightforward. However, if the acoustic mesh size is not consistent, a more complicated procedure is required to obtain the area for each element.

Chapter 4 presents the results obtained using this methodology.

# Chapter 4

# Results & Discussion

The results of the parametric study of the designs listed in Table 3.1 are presented in this chapter. Analysis of surface-averaged acceleration and surface-averaged sound power level is conducted for the CLT with acoustic black holes (ABH-CLT) and compared with the case of a CLT without ABH indentations (UNIFORM-CLT). In addition, the acoustic response is reported in the third octave band. A parametric study reveals the general trends when the number of indentations and the outer radius. This can be complemented with an optimization study when considering a specific applications.

## 4.1 Effect of the number of indentations

The structural response of the UNIFORM-CLT serves as a baseline for comparison against the ABH-CLT. Notably, engineered wood like CLT exhibits higher material damping compared to metals, with a loss factor of 0.02 for wood compared to 0.001 for aluminum [12], [38]. While the literature on ABH generally suggests their benefits when accompanied by a thin dissipative material in the retarding region [12], [27], [36], these studies have predominantly focused on materials with negligible material damping. Therefore, considering a material with inherent damping characteristics, such as wood, requires a careful approach. Initially examining the effect of ABH without added damping in the retarding region may be beneficial.

Altering the geometrical properties of a structure affects its structural frequency response. In

this section the number of periodic ABH indentations are increased gradually in order to observe trends in the structural response. Figures 4.1 - 4.4 illustrate how the steady-state surface averaged acceleration of a UNIFORM-CLT floor compares with an ABH-CLT floor as the number of indentations increases from 4 to 25 in each ply. The outer radius, $R$, has been fixed to 150 mm, and no additional damping is applied in the retarding region. The cut-on frequency of a single-cell ABH is used to estimate the cut-on frequency of the ABH-CLT floor [39]

$$f_{cut-on} = \frac{\pi h_0}{4R_{ABH}^2}\sqrt{\frac{E_z}{3\rho(1-\nu^2)}} \tag{31}$$

At R = 150 mm, the cut-on frequency is 640 Hz, with the corresponding regions highlighted in green. Figure 4.1 compares the steady-state frequency response of the 4-ABH with the uniform CLT, showing largely similar response curves. Above 640 Hz, the response of 4-ABH deviates from that of the uniform CLT. While existing literature emphasizes the attenuation benefits that can be gained after the cut-on frequency has been reached [12], [27], [36], these benefits are not apparent in the absence of additional damping in the ABH region.

As the number of indentations increases, the frequency response further deviates from that of the UNIFORM-CLT, with unpredictable trends occurring both above and below the cut-on frequency. Figure 4.2 compares the response of the 9-ABH configuration with that of the UNIFORM-CLT, revealing more resonance peaks than observed in the 4-ABH case. Similarly, increased resonance peaks are observed in the response curves of the 16-ABH and 25-ABH configurations, as shown in Figures 4.3 and 4.4, respectively.

The deviation of the frequency response from a UNIFORM-CLT floor can be attributed to various factors, including the reduced floor mass and the impact of the cut-on frequency, among others. These factors collectively contribute to the challenge of capturing trends in the structural response when the number of indentations is gradually varied.

The cut-on frequency can be visually verified by inspecting the deflection shapes. Figure 4.5 shows the deflection shapes of the UNIFORM-CLT, 4-ABH, 9-ABH, 16-ABH, and 25-ABH at 500 Hz, 640 Hz, and 857 Hz. Below the predicted cut-on frequency at 500 Hz, the deflection

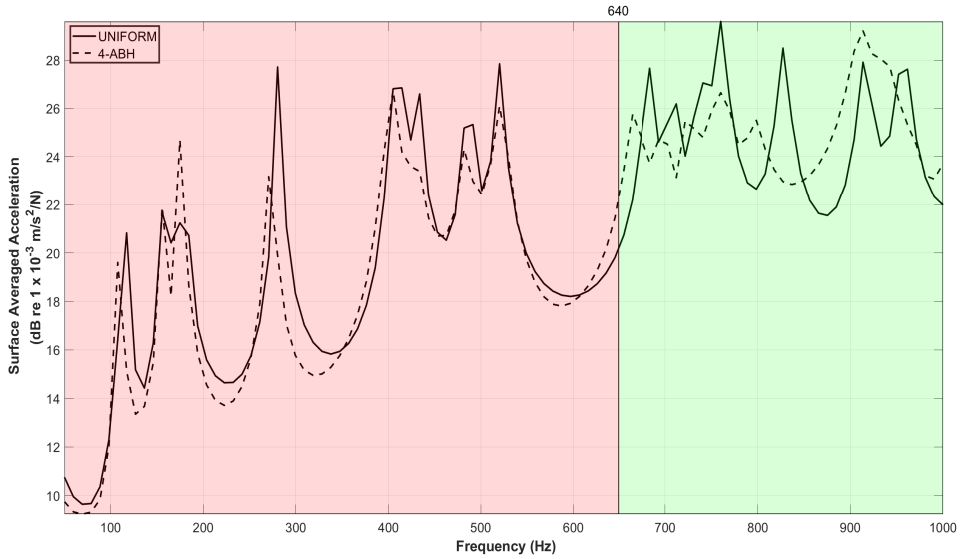


Figure 4.1: Surface averaged acceleration of the UNIFORM-CLT and 4-ABH at $R = 150mm$

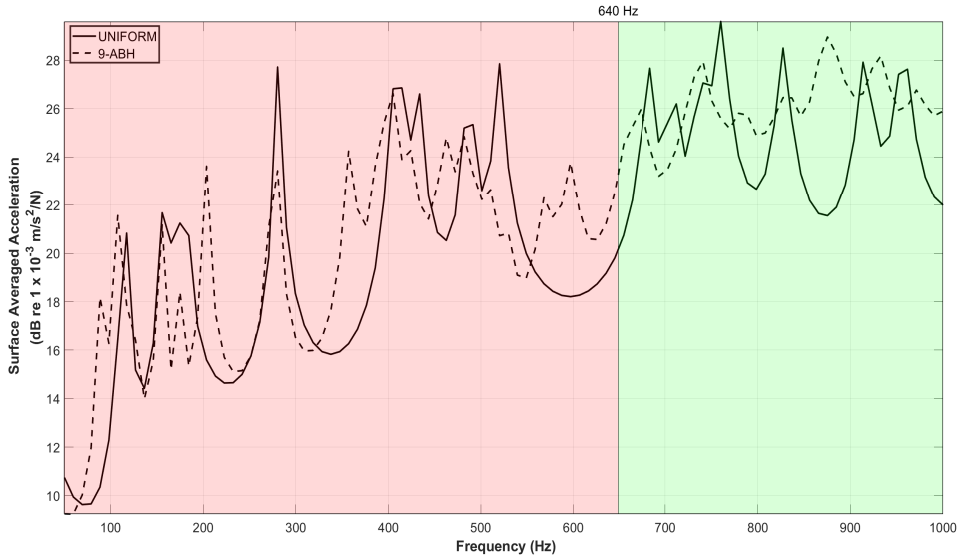


Figure 4.2: Surface averaged acceleration of the UNIFORM-CLT and 9-ABH at $R = 150mm$

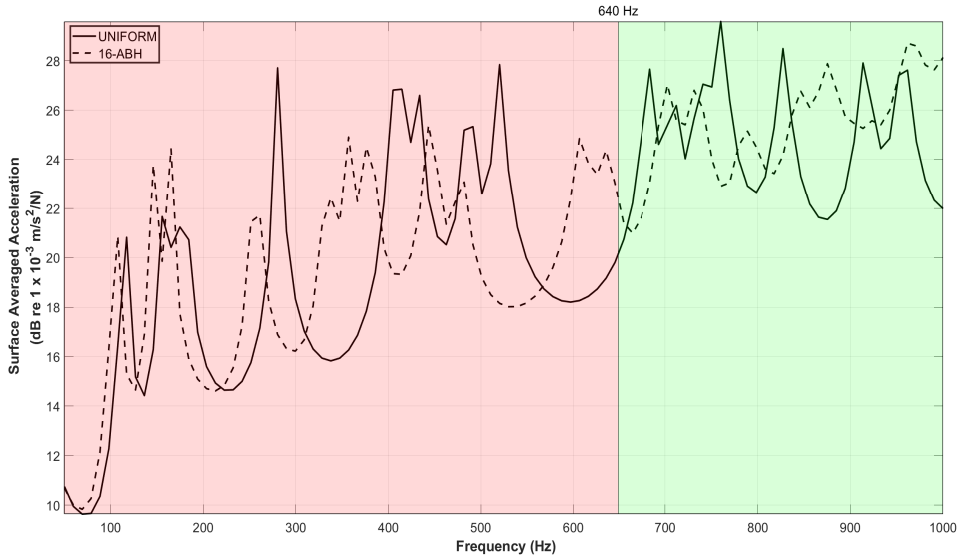


Figure 4.3: Surface averaged acceleration of the UNIFORM-CLT and 16-ABH at $R = 150mm$

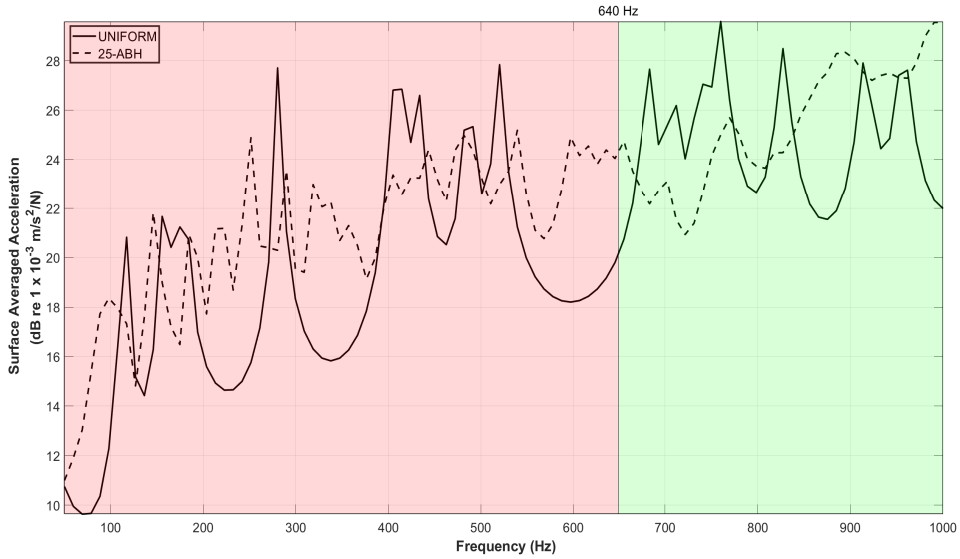


Figure 4.4: Surface averaged acceleration of the UNIFORM-CLT and 25-ABH at $R = 150mm$

shapes exhibits a characteristic bending and twisting pattern similar to that found in the UNFIORM-CLT. Beyond the cut-on frequency, at 857 Hz, the deflection shapes show maximum displacements concentrated in the retarding regions. This observation confirms the contribution of the cut-on frequency to structural response of the CLT floor.

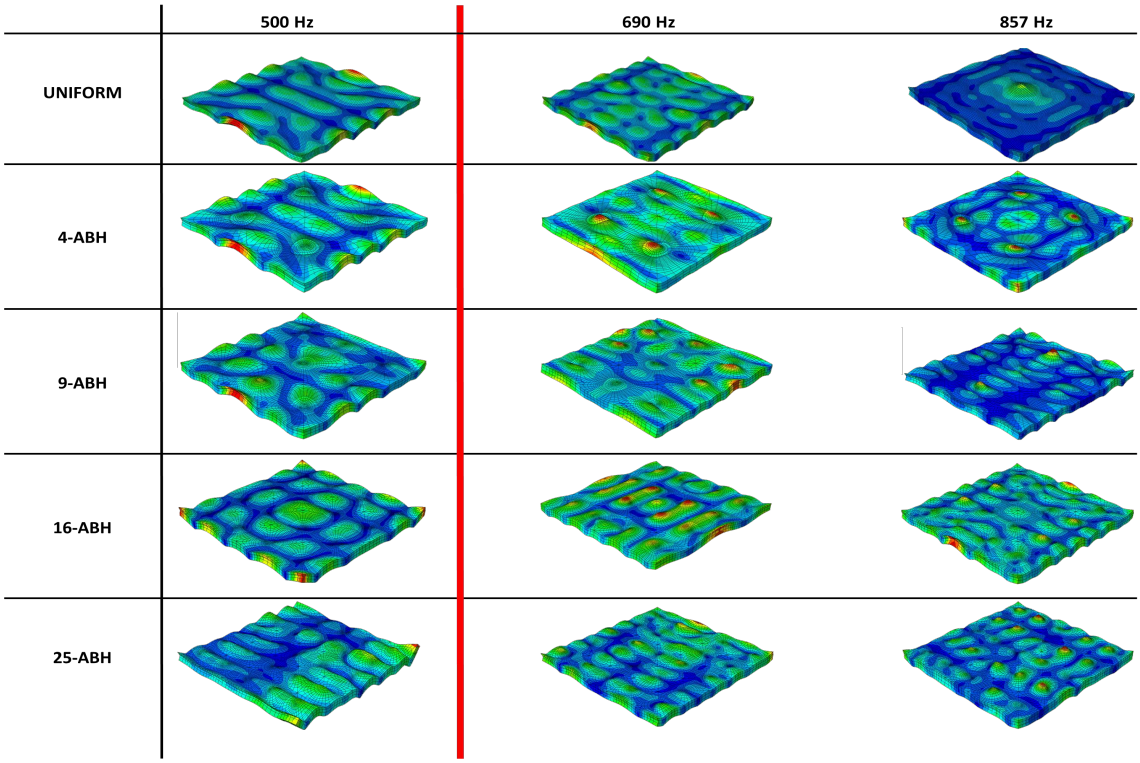


Figure 4.5: Operating deflection shapes of the UNIFORM-CLT and ABH-CLT at 500 Hz, 690 Hz and 857 Hz, and $R = 150mm$. The single-cell cut-on frequency is 640 Hz

Higher amplitudes at the ABH centers are anticipated based on theories presented in the literature. This local amplification facilitates efficient energy transfer to the damping layer. However, in this case where no additional damping is applied in the retarding region, energy is retained in the structure as there is noe medium to dissipate it. For a fixed radius, increasing the number of indentations offers the opportunity to activate more holes. However, it is not clear if the effects are advantageous or detrimental to the acoustic response. The design question revolves around whether the benefits of increasing the number of indentations outweigh those of increasing the outer radius. For instance, the 4-ABH configuration allows for larger radii values that are unattainable by the 25-ABH configuration due to geometric constraints, highlighting the trade-offs involved in choosing

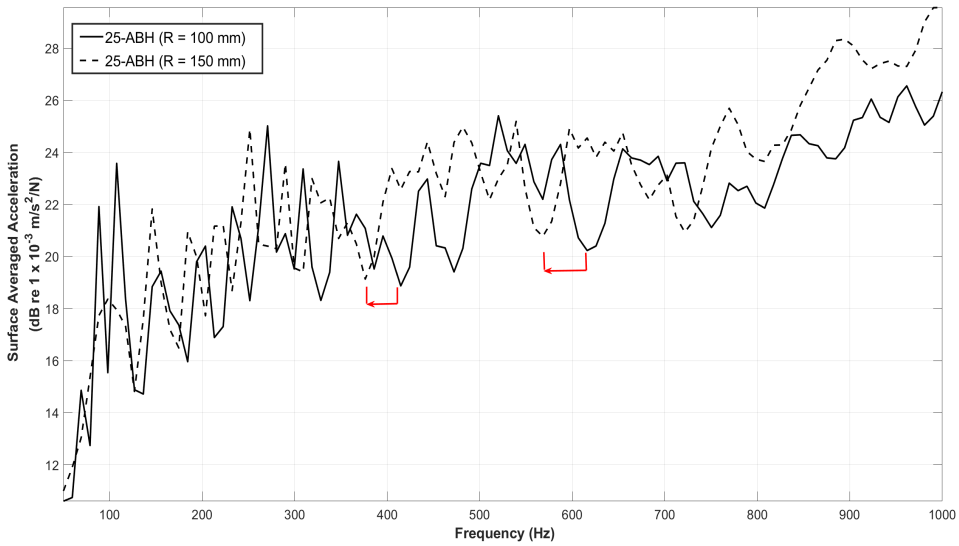


Figure 4.6: Surface averaged acceleration of the 25-ABH for radii values, $R$ of 100 mm and 150 mm

between these two design parameters.

## 4.2 Effect of the outer Radius

The structural response can also be influenced by varying the outer radius, $R$. Figure 4.6 shows the frequency response of the 25-ABH for $R$ values of 100 mm and 150 mm. The cut-on frequencies are 1433 Hz and 640 Hz, respectively. Although the response profiles of both configurations are similar, increasing $R$ from 100 mm to 150 mm shifts the overall response to lower frequencies. This shift also verifies the fact that a lower cut-on frequency is achieved by increasing the radius. However, shifting resonance points towards lower frequencies is generally not recommended because it is difficult to damp at low frequencies[4]. Figure 4.7 shows no displacement concentration in the retarding region at 857 Hz when $R$ is 100 mm, indicating that the cut-on frequency has not been reached.

The outer radius is varied in multiple steps to observe the structural response. To facilitate visual comparison, the response of the UNIFORM-CLT is extrapolated to a surface plot, illustrated in Figure 4.8. Subsequently, Figures 4.9- 4.12 present surface plots showing the surface-averaged

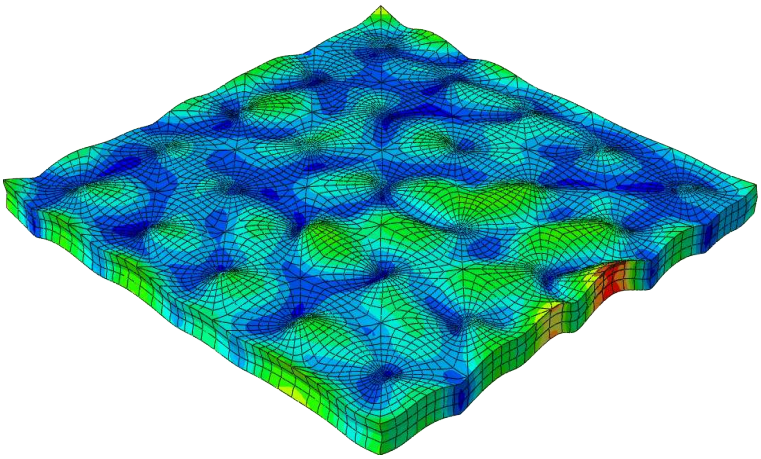

Figure 4.7: Operating deflection shape of the 25-ABH with $R = 100mm$ at 857 Hz

acceleration for the 25-ABH, 16-ABH, 9-ABH, and 4-ABH respectively as a function of $R$.

In Figure 4.9, the response of the 25-ABH reveals a shift of resonance peaks towards lower frequencies with increasing $R$. The highlighted red region at the top is intended for visual comparison of the response above 640 Hz, previously identified as the cut-on frequency at 150 mm outer radius.

Figure 4.10 presents a similar surface plot for the 16-ABH, highlighting similar trends with increasing radius: a shift of resonance peaks towards lower frequencies. However, reducing the number of indentations further to 9-ABH and 4-ABH reveals a gradual convergence of the response profile towards that of a UNIFORM-CLT. This convergence is marked by resonance peaks becoming less sensitive to changes in radii values, resembling the response of the UNIFORM-CLT. The response profile of 4-ABH in Figure 4.12 has the closest resemblance to the uniform CLT, equally indicating that the influence of the ABH diminishes as the number of indentation decreases.

When the radii values of the 16-ABH, 9-ABH, and 4-ABH configurations are extended to 200 mm, 250 mm, and 400 mm, respectively, it reveals a more pronounced effect of increased radius. See Figures **??**

The highlighted red region at the top is intended to reflect the response above the cut-on frequency at the maximum radii value of each configuration. At $R$ of 200 mm the cut-on frequency is 358 Hz and the modal behaviour of the 16-ABH shows resonance peaks shift towards lower frequencies. The same occurs for the 9-ABH and 4-ABH with cut-on frequencies of 230 Hz and 90 Hz

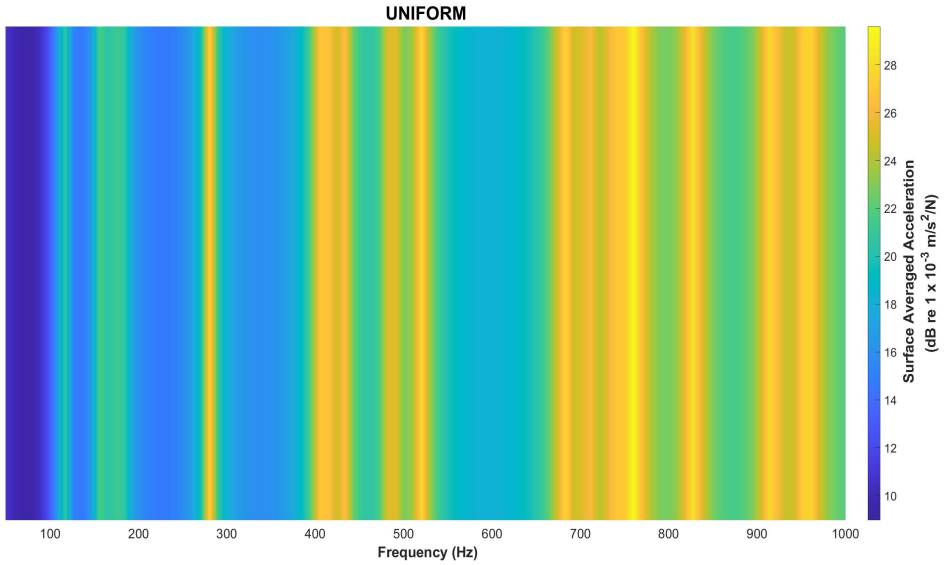


Figure 4.8: Surface averaged acceleration of the UNIFORM-CLT turned into a surface plot for visual comparison. Note that the response is only a function of frequency

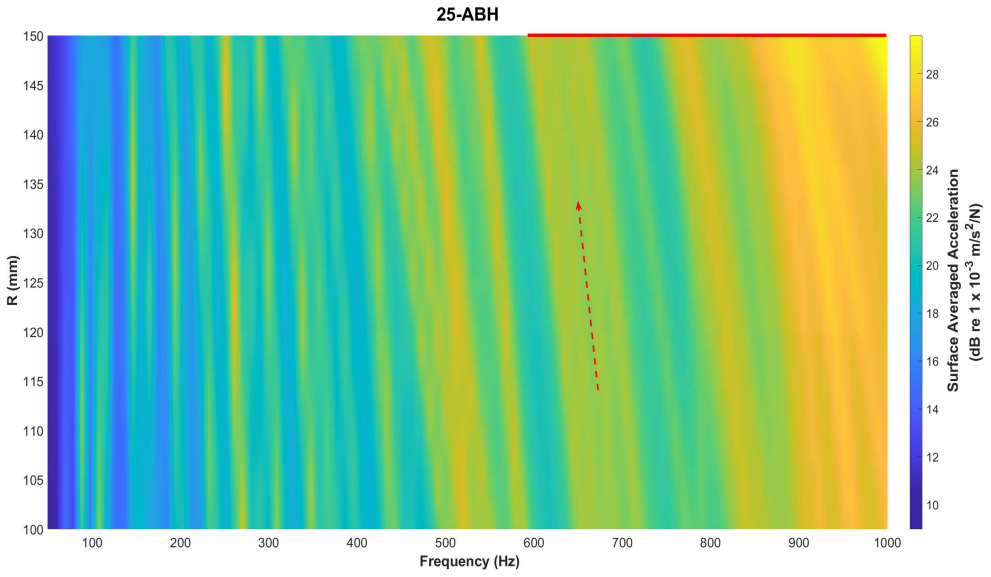


Figure 4.9: Surface averaged acceleration of the 25-ABH as a function of frequency and outer radius

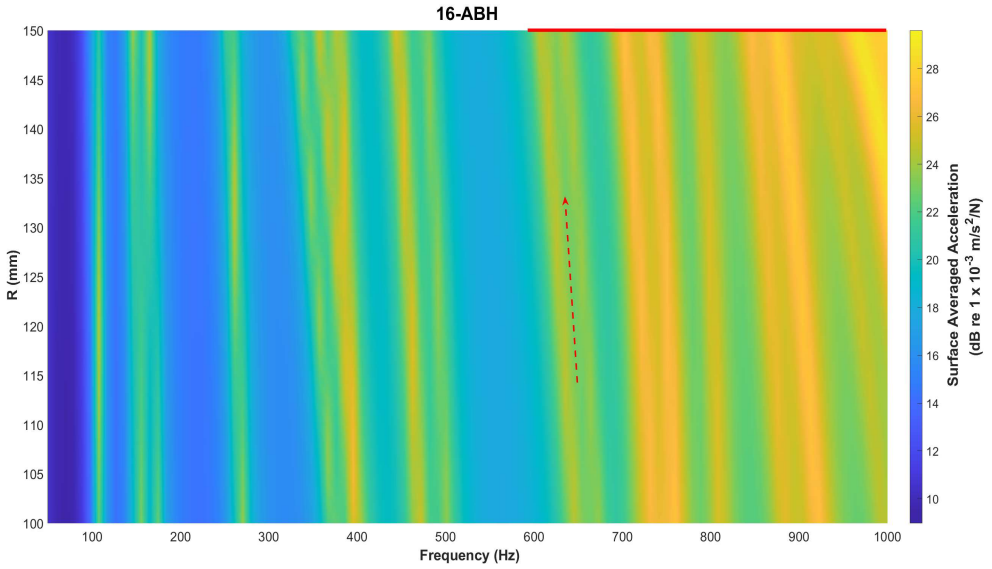


Figure 4.10: Surface averaged acceleration of the 16-ABH as a function of frequency and outer radius

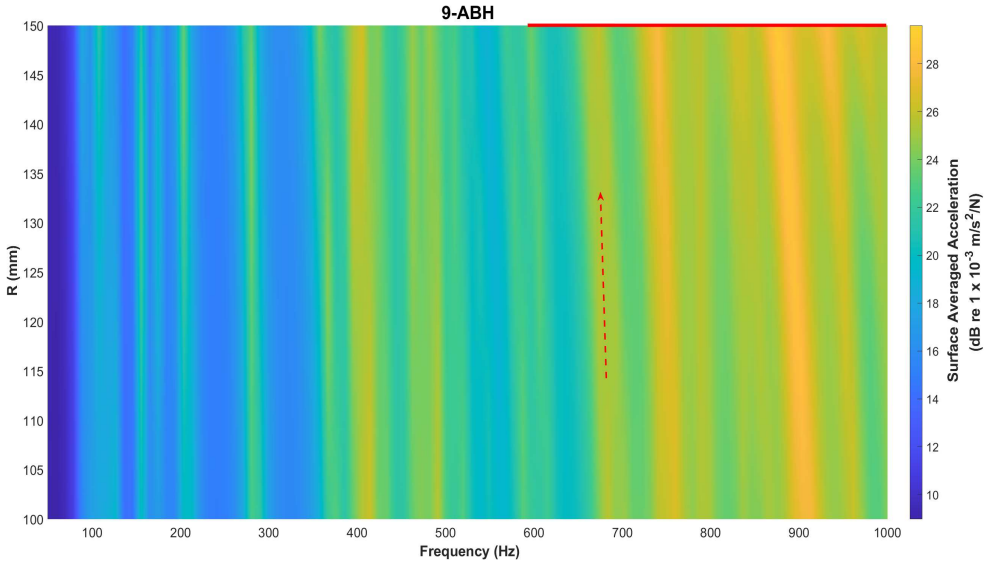


Figure 4.11: Surface averaged acceleration of the 9-ABH as a function of frequency and outer radius

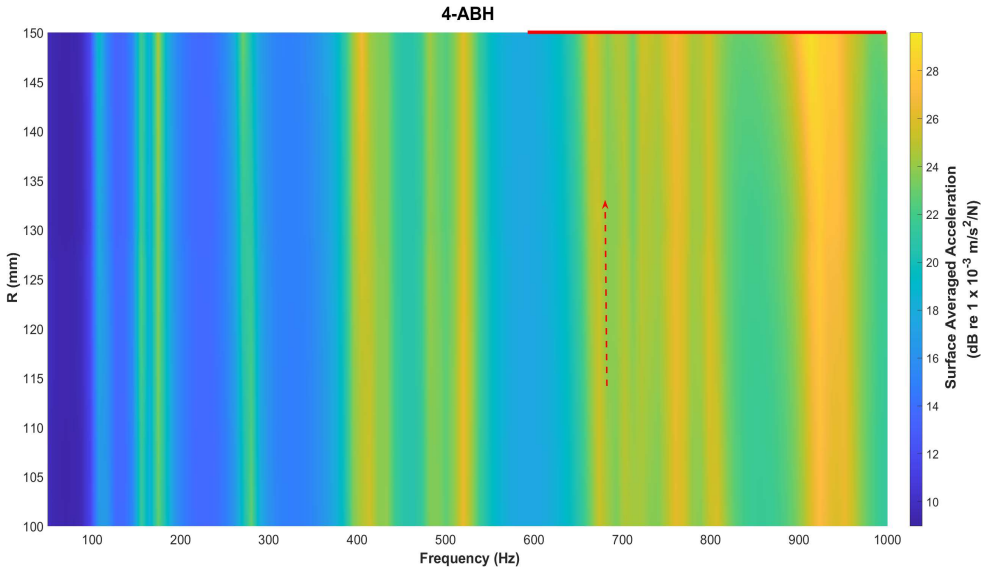


Figure 4.12: Surface averaged acceleration of the 4-ABH as a function of frequency and outer radius

respectively. Additionally, the shift towards lower frequencies appears to be nonlinear

## 4.3 Effect of structural damping

Structural damping plays a crucial role in reducing the response amplitude of a structure. Consequently, the performance of ABH can be enhanced by incorporating a damping layer into the retarding region [36]. In an ABH-CLT floor, this conceptually involves filling the holes with materials such as sand, elastomer, or concrete. In this work, the additional damping layer is incorporated in the finite-element model by increasing the structural loss factor in the ABH region. The main motivation for this approach is that it keeps the computational cost unchanged. However this approach makes a larger $R$ result in a larger damped volume. In addition, a non-structural mass is included in the ABH region to represent the mass of a damping material with negligible stiffness.

Figure 4.16 compares the contribution of damping to the surface-averaged acceleration of the 25-ABH and UNIFORM-CLT, both damped in identical regions. The influence of damping appears to be greater for the UNIFORM-CLT configuration compared to the 25-ABH configuration, with the damped UNIFORM-CLT achieving up to 5 dB reduction in response amplitude at $\eta = 0.03$,

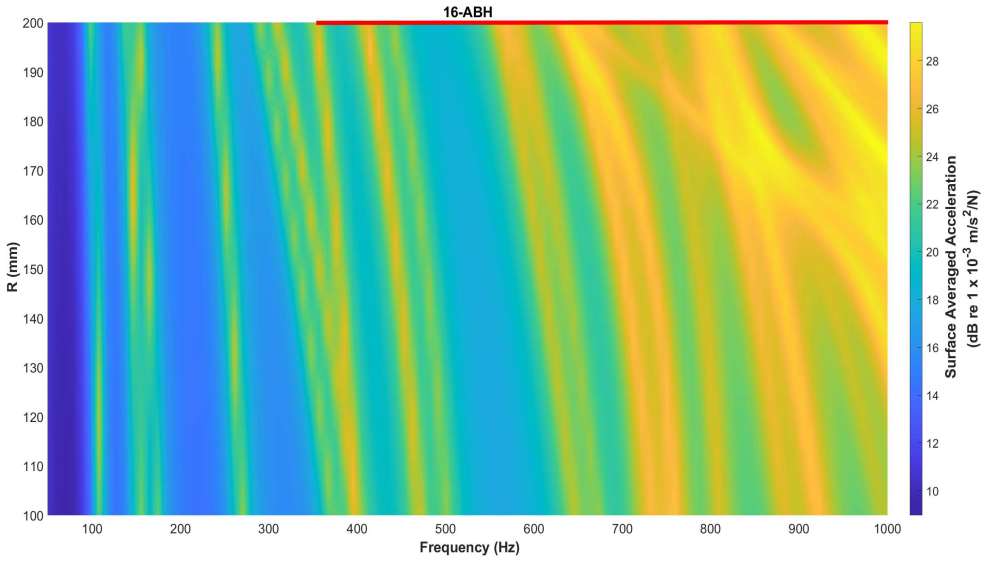


Figure 4.13: Surface averaged acceleration of the 16-ABH as a function of frequency and outer radius. The radii value is extended to the maximum outer radius that can be achieved by the 16-ABH

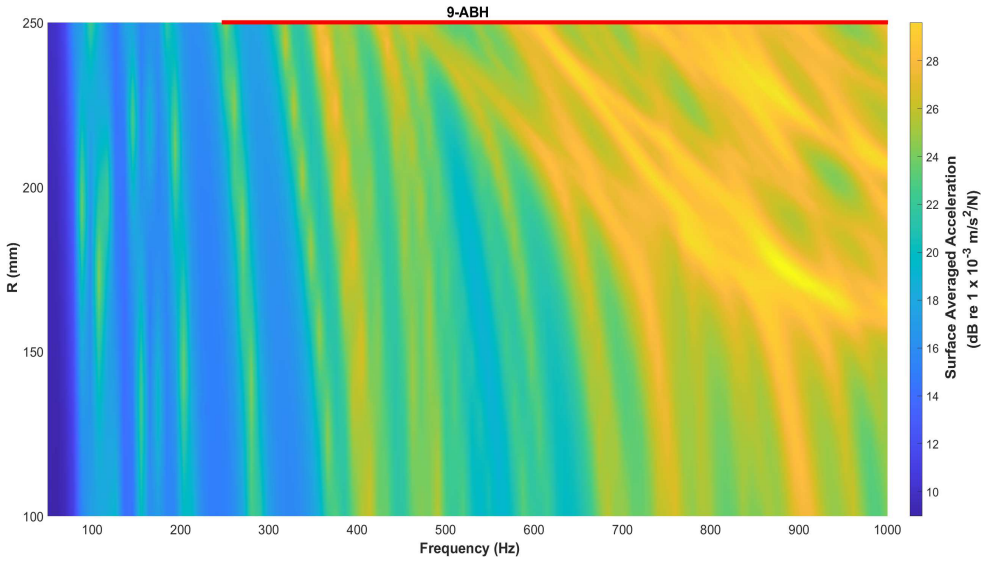


Figure 4.14: Surface averaged acceleration of the 9-ABH as a function of frequency and outer radius. The radii value is extended to the maximum outer radius that can be achieved by the 9-ABH

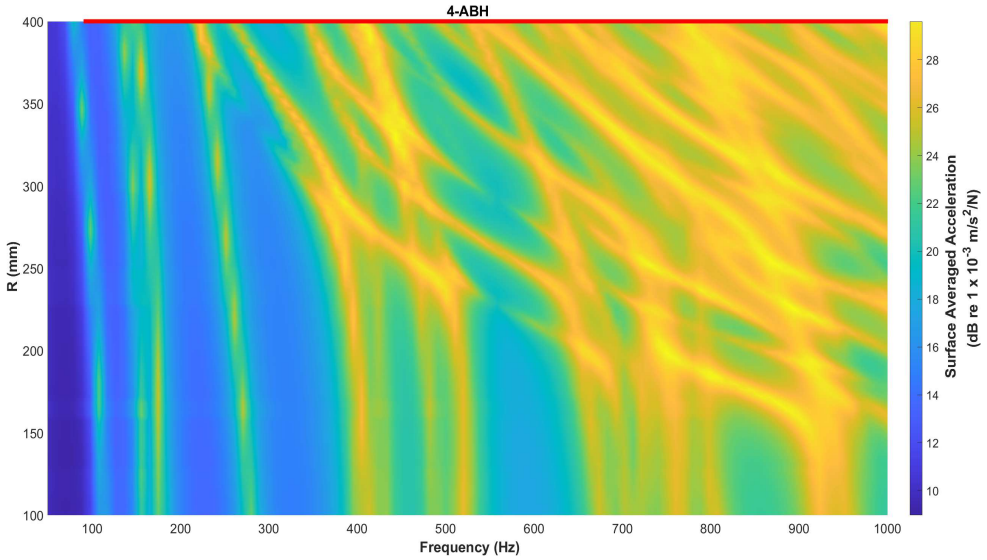


Figure 4.15: Surface averaged acceleration of the 4-ABH as a function of frequency and outer radius. The radii value is extended to the maximum outer radius that can be achieved by the 4-ABH

suggesting that it is more effective to damp the UNIFORM-CLT than the 25-ABH.

Figure 4.17 presents surface plots of the 25-ABH, 16-ABH, 9-ABH, and 4-ABH configurations with additional damping, illustrating the level of attenuation that can be achieved compared to the cases without damping. A conservative loss factor of 0.03 is chosen with the aim of approximating a thin dissipative layer. As expected, the largest changes are observed in the vicinity of resonances. However, the overall effect of damping is not significant for any of the configurations, with a maximum of 1.4 dB observed in the 4-ABH configuration. It means that the amount of damping required to attenuate the vibration within this frequency range is more important than the ABH geometry.

Thus far, the influence of damping appears to be proportional to the volume of damped elements in the numerical model, explaining why the damped UNIFORM-CLT achieves higher attenuation compared with the ABH-CLT. However, in practical scenarios, the addition of a damping material, such as sand, may produce different effects in the ABH-CLT and UNFIFORM-CLT. This necessitates further investigation into the influence of damping by separately modeling the damping layer and applying to corresponding regions of the ABH-CLT and UNIFORM-CLT.

In summary, in the absence of damping, no trend can be identified in the structural response

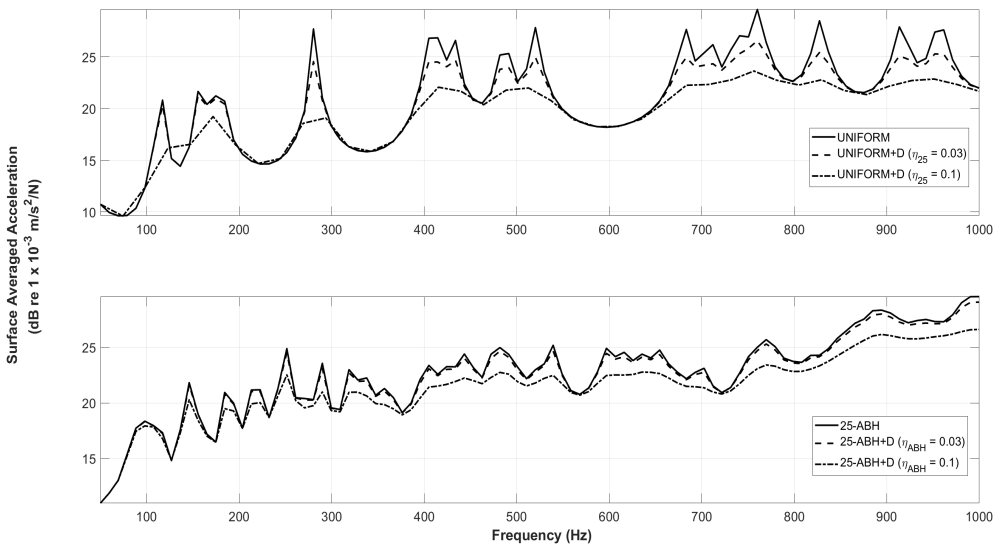


Figure 4.16: Surface averaged acceleration of the UNIFORM-CLT and 25-ABH with and without added damping. The loss factor in the ABH region is increased from 0.02 to 0.03. In turn, the UNIFORM-CLT is damped in similar region

when the number of indentations is increased. Meanwhile, a larger outer radius causes the frequency response to shift towards lower frequencies. With negligible damping of $\eta = 0.03$ only a maximum of 1.4 dB attenuation in surface mobility is observed, indicating that the amount of damping applied is more important than the ABH geometry if a reasonable amount of attenuation in vibration is desired. The following section considers the acoustic response of the ABH-CLT.

## 4.4 Examining the acoustic response

This section explores three parameters for examining the acoustic response: (i) A fixed outer radius which reveals the influence on the number of indentations (ii) Varied outer radius and (ii) Equivalent weight/damping of the CLT floor. Finally, the acoustic response is examined in a broad band.

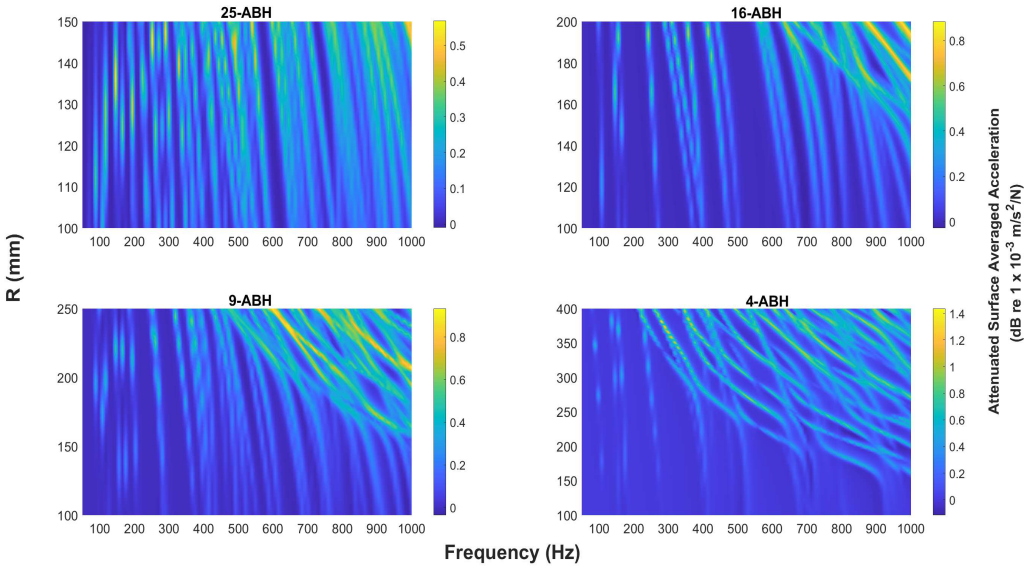


Figure 4.17: Attenuated surface averaged acceleration plotted as a function of frequency and outer radius when loss factor in the ABH region is increased from 0.02 to 0.03. The positive value indicates a reduction in surface averaged acceleration

### 4.4.1 Fixed outer radius

The influence of the number of indentations can be examined in the third octave band by fixing the outer radius as shown in Figure 4.18. While the resonance modes generated by the ABH appear problematic in the structural response, they adjust to generate lower sound power levels, compared with the UNIFORM-CLT, at higher center frequencies of 400 Hz and above. The attenuation achieved at higher center frequencies can be attributed in part to the relatively longer band bandwidth, highlighting the broadband efficiency of the ABH. Interestingly, the ABH-CLT can attenuate vibrations before the cut-on frequency, as in the case of $R$ at 150 mm, indicating that the acoustic performance cannot be predicted solely by the cut-on frequency.

However, there is no identifiable trend in the acoustic response as the number of indentations increases from 4 to 25. Therefore, maximizing the number of indentations might not improve the acoustic performance of the floor. However, at higher damping values of $\eta = 0.2$, the response adjusts to favour maximizing the number of indentations, see Figure 4.19.

Below 400 Hz the sound power radiated from the ABH-CLT is not consistently below the sound

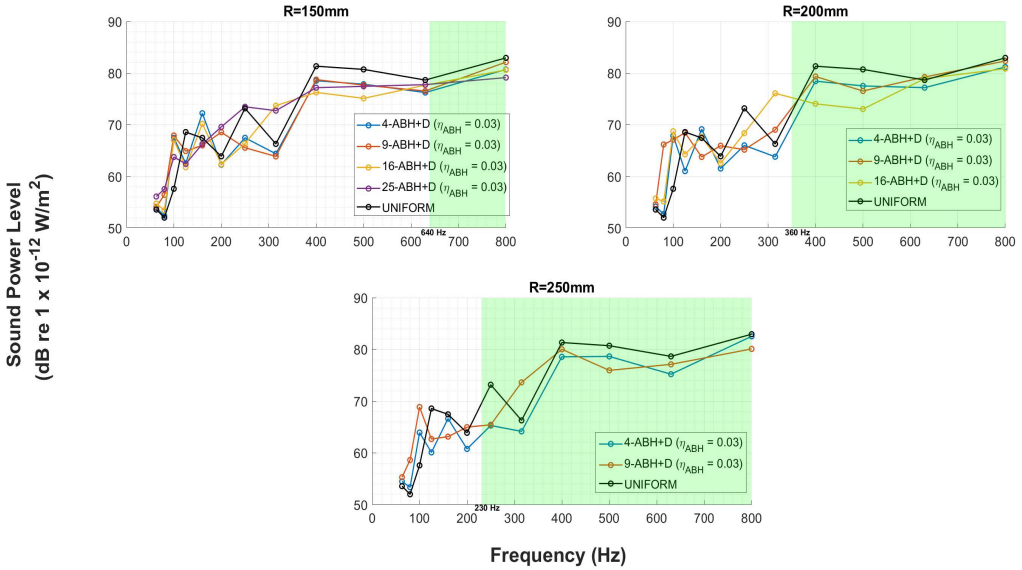


Figure 4.18: Sound power level of the UNIFORM-CLT and ABH-CLT for fixed outer radius at $\eta = 0.03$. The green area signifies the region above the cut-on frequency

power radiated from the UNIFORM-CLT, regardless of the amount of damping applied in the retarding region. This implies that incorporating the ABH is not feasible for mitigating impact noise at frequencies below 400 Hz.

### 4.4.2 Variable Outer Radius

Similarly, the outer radius is varied for a fixed number of indentation, as shown in Figure 4.20. There is consistent attenuation in radiated sound power at higher centre frequencies of 400 Hz and above, but no trend in the acoustic response as the outer radius is increased. However, when the damping value is increased to $\eta = 0.2$ the response favours maximizing the outer radius, see Figure 4.21.

Generally, the acoustic response is dictated by the amount of damping applied. At a structural loss factor of 0.03, there is no marginal improvement in acoustic response by maximizing the outer radius even though this helps to decrease the cut-on frequency. However, when the structural loss factor is increased to 0.2, then the response favours maximizing the outer radius. Nevertheless, it can be demonstrated that this trend is attributed to an increase in the volume of the damped

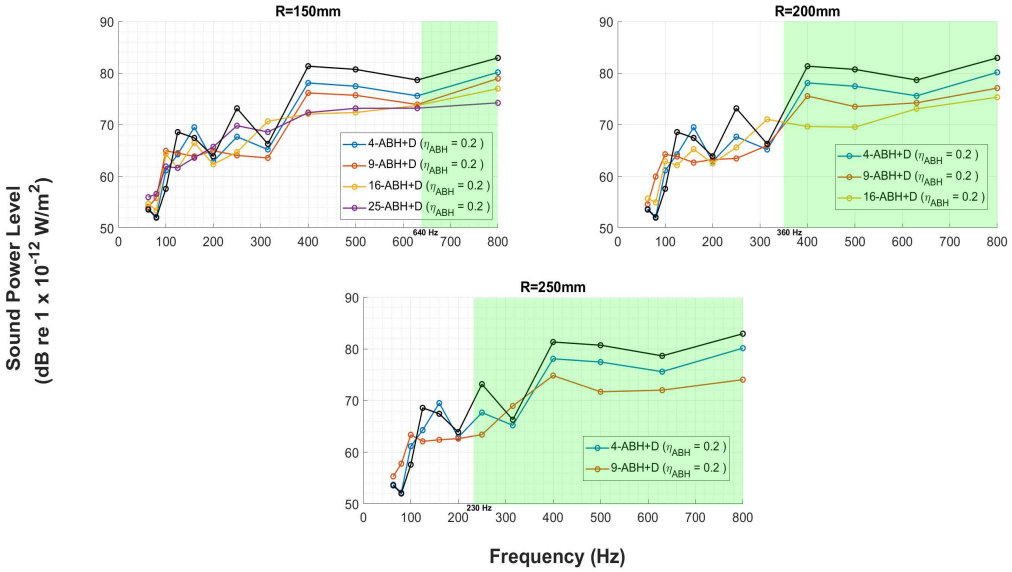


Figure 4.19: Sound power level of the UNIFORM-CLT and ABH-CLT for fixed outer radius at $\eta = 0.2$. The green area signifies the region above the cut-on frequency

region. Consider the following section where the 25-ABH, 16-ABH, 9-ABH and 4-ABH are equally damped

### 4.4.3 Equivalent Weight

In this section, the 25-ABH at 150 mm serves as a baseline for this acoustic analysis. The objective ensure an equivalent weight in the 16-ABH, 9-ABH, and 4-ABH configurations, resulting in radii values of 180 mm, 240 mm and 340 mm respectively. This design naturally ensures that the volume of damped elements across the configuration stays the same. The UNIFORM-CLT is damped in identical regions for a fair comparison. For example, in the case of the 25-ABH at 150 mm, the UNIFORM-CLT is damped in 25 regions at the same radius.

Figure 4.22 provides a comparison of the acoustic response between the damped 25-ABH, 16-ABH, 9-ABH, 4-ABH and the UNIFORM-CLT, both with and without added damping, all reported in the third-octave band. The structural loss factor is set to 0.03 which has previously been established to be negligible.

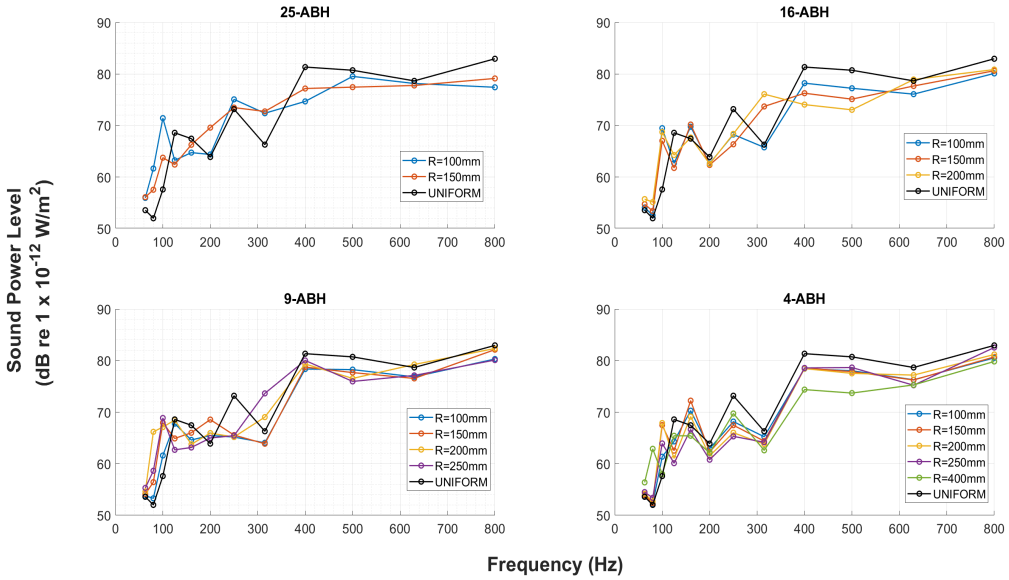


Figure 4.20: Sound power level of the UNIFORM-CLT and ABH-CLT for various radii values, in the third octave band at $\eta = 0.03$

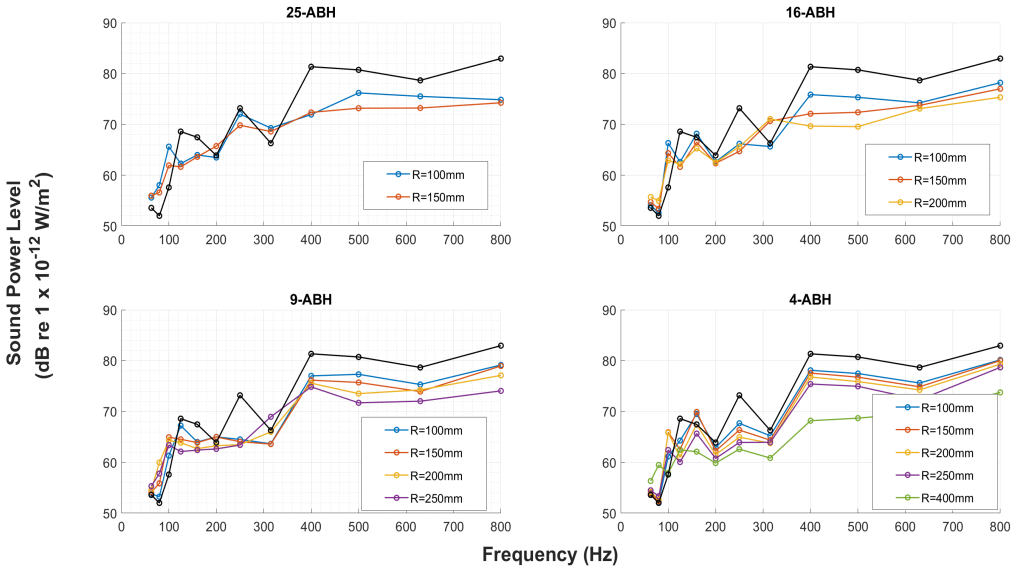


Figure 4.21: Sound power level of the UNIFORM-CLT and ABH-CLT for various radii values, in the third octave band at $\eta = 0.2$

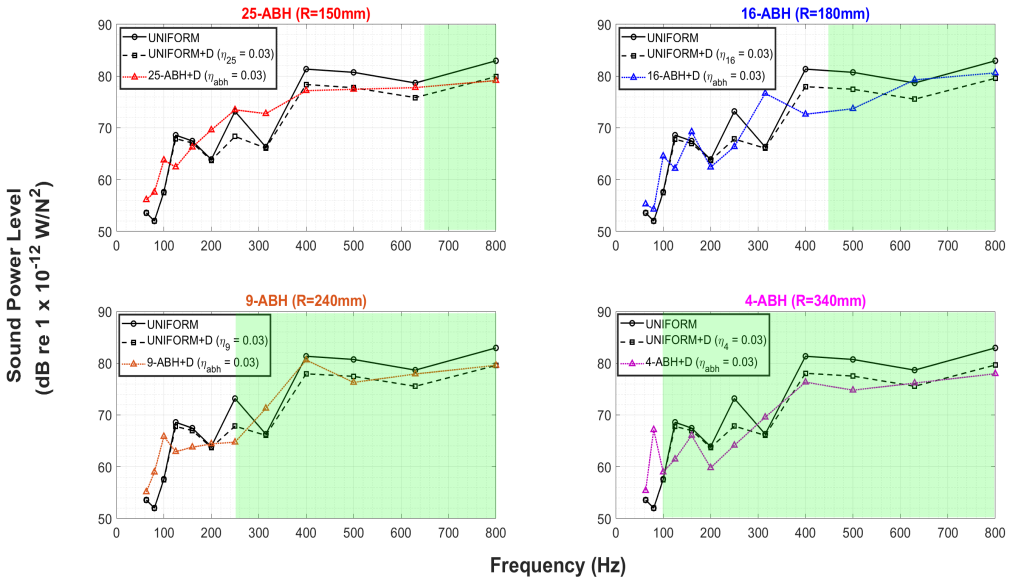


Figure 4.22: Sound power level of the UNIFORM-CLT (UNIFORM), damped UNIFORM-CLT (UNIFORM-CLT+D) and damped ABH; 25-ABH+D(Topleft), 16-ABH+D(Topright), 9-ABH+D(Bottomleft), 4-ABH+D (Bottomright). A damping value of 0.03 is applied to the retarding regions and corresponding regions in UNIFORM-CLT+D. The green areas signify the region above the cut-on frequency

The damped UNIFORM-CLT achieves similar attenuation above 400 Hz as the damped 25-ABH. The same response characteristics are observed in the 16-ABH, 9-ABH, 4-ABH and damped UNIFORM-CLT. Therefore it is shown that there is no added advantage in incorporating ABH because the important factor is the amount of damping added to the CLT floor to attenuate the vibrations, hence the radiated sound. Interestingly, the response of the damped UNIFORM-CLT remains unaffected by the specific areas where damping is applied; as long as the volume of the damped element is the same. When, the structural loss factor is increased to 0.2,see Figure 4.23 they all show similar performance above 400 Hz, despite having different radius or cut-on frequencies.

### 4.4.4 Broadband Analysis

In the third-octave band, the effect of varying the radius or number of indentations may not be apparent. It has already been shown that the acoustic performance of the ABH improves at higher centre frequencies which have longer band lengths, this motivates the case to examine a broadband.

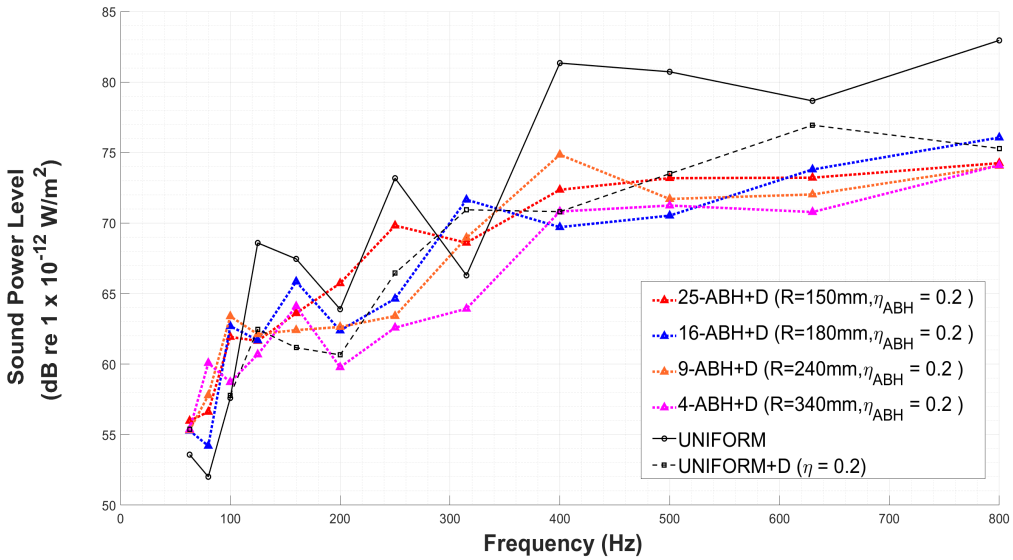


Figure 4.23: Sound power level of the UNIFORM-CLT (UNIFORM), damped UNIFORM-CLT (UNIFORM-CLT+D) and damped ABH; 25-ABH+D(Topleft), 16-ABH+D(Topright), 9-ABH+D(Bottomleft), 4-ABH+D (Bottomright). A damping value of 0.2 is applied to the retarding regions and corresponding regions in UNIFORM-CLT+D

Figure 4.24 shows the attenuation of the unweighted sound power level compared to UNIFORM-CLT, as a function of radius, reported in two broadbands: $L_{i,50-600}$ and $L_{i,50-800}$. The positive value indicates that the UNIFORM-CLT has a higher sound power level within the band. The results show all values being positive. More importantly, it also shows that the acoustic broadband reponse of the ABH-CLT floor does not follow a trend that supports maximizing the number of indentations or the outer radius, rather it shows that the number of indentations or outer radius can be optimized. Meanwhile, when the damping value is increased to $\eta = 0.2$, the response now follows a trend that favours maximizing the number of indentations as well as the outer radius. More importantly, it reveals that the attenuation favors maximizing the volume of the damped region, as depicted in Figure 4.25.

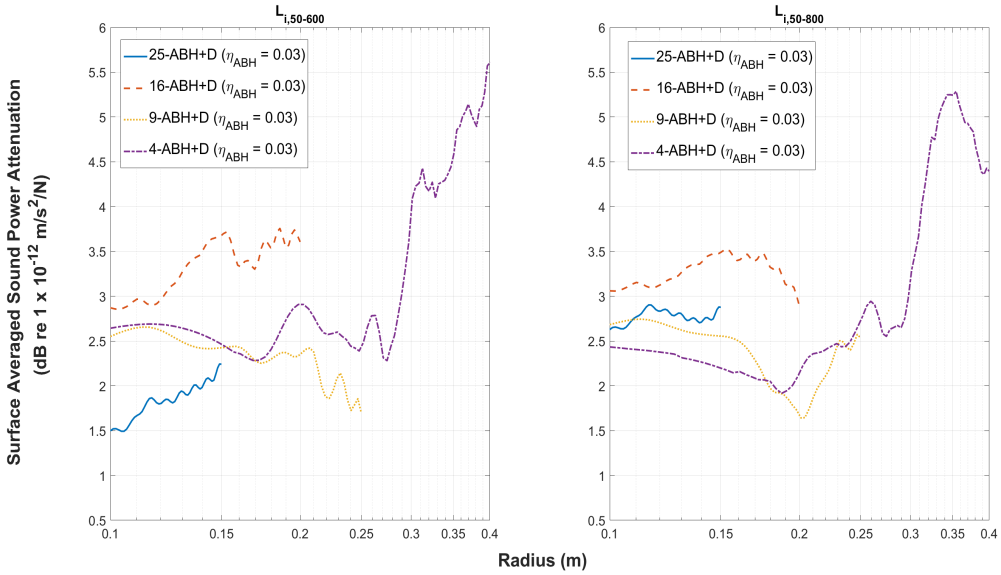


Figure 4.24: Surface averaged sound power attenuation as a function of radius at $\eta = 0.03$. The positive value indicates that the UNIFORM-CLT has a higher sound power level than the ABH-CLT

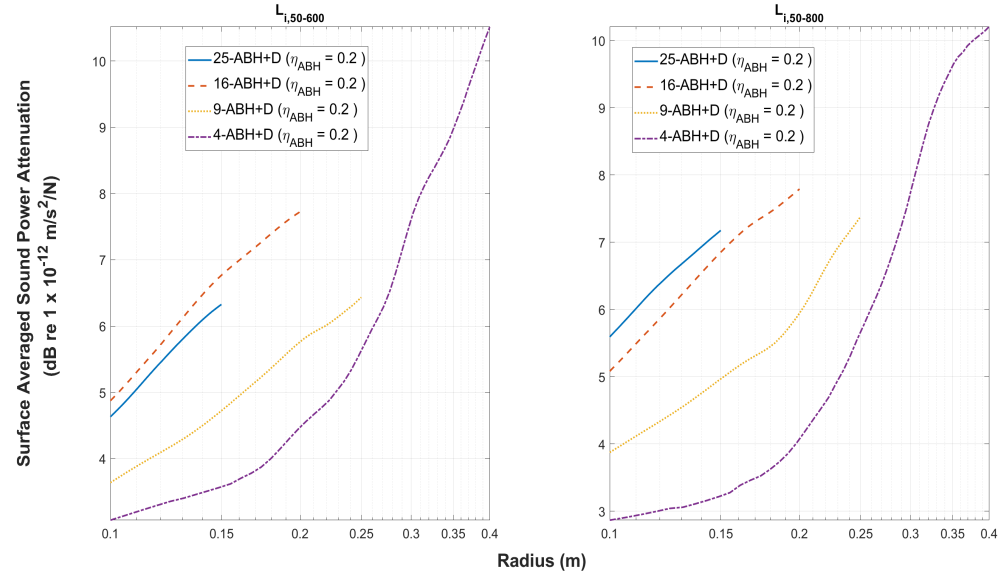


Figure 4.25: Surface averaged sound power attenuation as a function of radius at $\eta = 0.2$. The positive value indicates that the UNIFORM-CLT has a higher sound power level than the ABH-CLT

# Chapter 5

# Conclusion & Future Directions

## 5.1 Summary of Findings

This study primarily explores the potential of reducing impact noise in cross-laminated timber (CLT) within the 50-800 Hz range by embedding periodic grids of acoustic black holes (ABH) into CLT panels. The study examines the trends in vibro-acoustic response of the ABH-CLT when the number of indentations, outer radius, and structural damping is varied. Additionally, it evaluates the extent of sound attenuation that is achieved through the incorporation of ABH in CLT panels. The key findings are summarized as follows.

(1) Introduction of periodic grids of ABH alters the structural response of the uniform floor by creating resonant frequencies in the plate, as expected when the geometry of a structure changes. However these changes do not produce an identifiable trend due to the presence of other influential variables. This suggests that an optimization study may offer a more apt approach than a parametric study. Furthermore, the radiated sound power level is not reduced by maximizing the number of indentations, particularly when the retarding region exhibits negligible damping, characterized by a structural loss factor if 0.03. Conversely, when the damping value is increased to 0.2, the response favours maximizing the number of indentations. Nevertheless, this effect can be equally ascribed to the concurrent increase in the volume of damped regions.

(2) The cut-on frequency of the single-cell ABH plate provides a reliable estimate of the cut-on frequency of the ABH-CLT floor, evidenced by visually examining the deflection shapes. However, its utility to predict any improvement in acoustic performance is limited. For instance, reducing the cut-on frequency by enlarging the outer radius does not guarantee a reduction in radiated sound power, particularly when a loss factor of 0.03 was applied in the retarding region. Conversely, when the loss factor was increased to 0.2, the acoustic response favours maximizing the outer radius. Nevertheless, this observed behaviour can also be attributed to an increase in volume of the damped region.

(3) Consistent attenuation in sound power level in the ABH-CLT is observed at higher center frequencies beyound 400 Hz, motivating the case for a broadband analysis in the range: $L_{i,50-600}$ and $L_{i,50-800}$. Examination within these frequency bands suggests that for scenarios with negligible damping of 0.03, the number of indentations can be optimized for a [articular outer radius. Equally an increase in outer radius does not guarantee improvement in attenuation. However, with an increase in the loss factor to 0.2, the broadband response now indicates a preference for maximizing both the number of indentations and the outer radius. Crucially, it now emphasizes the importance of maximizing the volume of the damped region. Hence, it appears that the vibro-acoustic response of the ABH-CLT within the 50-800 Hz range is predominantly influenced by the level of damping present in the floor rather than the geometric characteristics of the ABH.

(4) Below the center frequency of 400 Hz, there is a lack of consistent attenuation in the sound power level of the ABH-CLT, irrespective of the configuration of the ABH and the damping applied in the ABH region. This observation underscores the limited effectiveness of ABH in mitigating impact noise within these frequency ranges

The study acknowledges the following limitations:

(1) The numerical model assumes the mass of the dissipative layer in the ABH region to be negligible, aligning with existing literature directives that emphasize the inclusion of a lightweight damping material in the ABH region for analytical focus on ABH geometry rather than mass

considerations [36]. However, it is important to note that the definition of what constitutes "light" damping material remains somewhat ambiguous.

(2) The application of the force disturbance is not consistent across the various ABH-CLT configurations. For instance, while the force disturbance was centered in the case of UNIFORM-CLT, 4-ABH, and 16-ABH configurations, it was offset by 0.2m and 0.66m in the cases of 25-ABH and 9-ABH configurations, respectively. Such discrepancies can lead to an unfair comparison in the response curves

(3) The numerical model does not represent a detailed setup of standardised impact noise tests such as ASTM E989-06 [6] and ISO 717-2(2020) [33]. Rather, the aim is to compare the performance of a CLT floor with and without ABH indentations to observe attenuation in the vibro-acoustic response, with the intention of motivating future experimental investigations. This approach simplifies the model, facilitating a parametric study. The methodology for the numerical model and solution procedure draws inspiration from similar methodologies outlined by Hook et al. [27] and Conlon et al. [12].

(4) As the numerical model does not replicate a standardized impact noise test, the focus is not solely on the absolute sound power level, but rather on the trends in sound power level as the parameters are varied, and the extent of sound power level attenuation achievable when ABH indentations are integrated into the CLT floor.

(5) This work does not seek to calibrate the mechanical properties of CLT using an experimental model. Instead, the mechanical properties of the CLT have been derived directly from Yang et al. [38]. It is acknowledged that, in practice, validating these mechanical properties through experiments is necessary given the properties of wood which are dependent on diverse factors such as the region where the tree was harvested and uncertainties induced during manufacturing.

## 5.2 Future Directions

This study motivates several directions for future studies exploring the potential for integrating ABH indentations within CLT to mitigate impact noise. Some of the suggestions include:

(1) **Modeling the dissipative layer:** In the current numerical model, additional damping was incorporated by adjusting the material properties of the ABH region. Similarly, the UNIFORM-CLT was damped in corresponding areas to ensure a fair comparison. This approach, while efficient computationally, may benefit from further refinement in future studies. One potential direction involves developing a separate model specifically dedicated to simulating the behavior of the lossy material, thus enhancing the damping model.

(2) **Footstep spectra:** In this study, the input force is modeled as a steady state harmonic force. This approach is chosen to highlight the steady-state sound power attenuation derived by incorporating ABH; this can be converted into the effective transfer function of the floor. However, to enhance the direct relevance of the simulations, future work could involve incorporating a realistic spectrum of footstep impact on wooden floors in the time domain. This approach would also provide insights into other aspects of the response, such as the settling time.

(3) **CLT modeling:** The analysis can be extended to encompass more resilient scenarios, such as implementing compliant boundary conditions as opposed to free boundaries considered in this study. This extension would enable an examination of the influence of practical construction aspects on the ABH

(4) **ABH location:** This study focuses on the periodic placement of ABH on a plate. However, there may be potential for optimization in the placement of ABH, which could be explored in future investigations.

(5) **Room acoustic simulation:** To offer a more comprehensive insight into the effectiveness of ABH in mitigating impact noise, modeling the acoustics in the receiving room and validating them through impact noise assessments could be beneficial. By coupling this approach

with a realistic frequency spectrum of footstep noise, as mentioned earlier, room acoustic simulations can facilitate the auralization of footstep noise within the receiving room. This would provide a more detailed understanding of how ABH influences the overall impact noise environment.

# References


[1] K. Bodlund, "Alternative reference curves for evaluation of the impact sound insulation between dwellings," *Journal of sound and vibration*, vol. 102, no. 3, pp. 381–402, 1985.

[2] M. Mironov, "Propagation of a flexural wave in a plate whose thickness decreases smoothly to zero in a finite interval," *Sov. Phys. Acoust*, vol. 34, no. 3, pp. 318–319, 1988.

[3] A. Warnock, "Controlling the transmission of impact sound through floors," 1999. DOI: 10.4224/40002834. [Online]. Available: https://doi.org/10.4224/40002834.

[4] T. L. Schmitz and K. S. Smith, *Mechanical vibrations modeling and measurement*, 2001.

[5] V. Krylov, "Propagation of plate bending waves in the vicinity of one-and two-dimensional acoustic 'black holes'," 2007.

[6] S. E33.03, *Standard classification for determination of impact insulation class (iic)*, 2012. DOI: 10.1520/E0989-06. [Online]. Available: https://www.astm.org/e0989-06.html.

[7] C. Hopkins, *Sound insulation*. Routledge, 2012.

[8] R. Öqvist, F. Ljunggren, and A. Ågren, "On the uncertainty of building acoustic measurements–case study of a cross-laminated timber construction," *Applied Acoustics*, vol. 73, no. 9, pp. 904–912, 2012.

[9] A. Climente, D. Torrent, and J. Sánchez-Dehesa, "Gradient index lenses for flexural waves based on thickness variations," *Applied Physics Letters*, vol. 105, no. 6, 2014.

[10] V. Krylov, "Acoustic black holes: Recent developments in the theory and applications," *IEEE Transactions on Ultrasonics, Ferroelectrics, and Frequency Control*, vol. 61, pp. 1296–1306, 8 2014, ISSN: 0885-3010. DOI: 10.1109/TUFFC.2014.3036. [Online]. Available: https://ieeexplore.ieee.org/document/6863850.

[11] T. Sakuma, S. Sakamoto, and T. Otsuru, *Computational simulation in architectural and environmental acoustics*. Springer, 2014.

[12] S. Conlon, F. John, and S. Fabio, "Numerical analysis of the vibroacoustic properties of plates with embedded grids of acoustic black holes," *The Journal of the Acoustical Society of America*, vol. 137, pp. 447–457, 1 2015, ISSN: 0001-4966. DOI: 10.1121/1.4904501. [Online]. Available: https://pubs.aip.org/asa/jasa/article/137/1/447-457/911670.

[13] I. Sabourin, "Measurement of airborne sound insulation of 8 wall assemblies measurement of airborne and impact sound insulation of 29 floor assemblies," 2015. DOI: 10.4224/23000205. [Online]. Available: https://doi.org/10.4224/23000205.

[14] O. Aklouche, A. Pelat, S. Maugeais, and F. Gautier, "Scattering of flexural waves by a pit of quadratic profile inserted in an infinite thin plate," *Journal of Sound and Vibration*, vol. 375, pp. 38–52, 2016.

[15] N. Amiryarahmadi, W. Kropp, and K. Larsson, "Identification of low-frequency forces induced by footsteps on lightweight floors," *Acta Acustica united with Acustica*, vol. 102, pp. 45–57, 2016, ISSN: 16101928. DOI: 10.3813/AAA.918923. [Online]. Available: http://openurl.ingenta.com/content/xref?genre=article&issn=1610-1928&volume=102&issue=1&spage=45.

[16] Dassault Systèmes, *Abaqus documentation*, Version 6.16, Dassault Systèmes, John Wiley & Sons, 2016.

[17] S. E33.03, *Classification for rating sound insulation*, 2016. DOI: 10.1520/E0413-16. [Online]. Available: https://www.astm.org/e0413-16.html.

[18] J. H. Rindel, A. Løvstad, and R. Klæboe, "Aiming at satisfactory sound conditions in dwellings–the use of dose-response curves," in *Proc. Baltic-Nordic Acoustic Meeting, Stockholm*, 2016.

[19] *Acoustics — laboratory and field measurement of flanking transmission for airborne, impact and building service equipment sound between adjoining rooms — part 1-5*, International Organization for Standardization, 2017.

[20] D. Bard, J. Negreira, C. Guigou-Carter, *et al.*, "Modelling prerequisites-fem/sea impact and airborne sound (rise report 2017: 56)," *RISE Research Institutes of Sweden AB, Sweden*, 2017.

[21] M. Caniato, F. Bettarello, A. Ferluga, L. Marsich, C. Schmid, and P. Fausti, "Acoustic of lightweight timber buildings: A review," *Renewable and Sustainable Energy Reviews*, vol. 80, pp. 585–596, 2017.

[22] L. Tang and L. Cheng, "Broadband locally resonant band gaps in periodic beam structures with embedded acoustic black holes," *Journal of Applied Physics*, vol. 121, no. 19, 2017.

[23] T. Zhou, L. Tang, H. Ji, J. Qiu, and L. Cheng, "Dynamic and static properties of double-layered compound acoustic black hole structures," *International Journal of Applied Mechanics*, vol. 9, no. 05, p. 1 750 074, 2017.

[24] D. Bies, C. Hansen, and C. Howard, *Engineering noise control*. CRC Press, Taylor & Francis Group, 2018, ISBN: 978-1-4987-2405-0.

[25] W. Huang, H. Ji, J. Qiu, and L. Cheng, "Analysis of ray trajectories of flexural waves propagating over generalized acoustic black hole indentations," *Journal of Sound and Vibration*, vol. 417, pp. 216–226, 2018.

[26] *Acoustics — measurement of floor impact sound insulation of buildings — part 2: Method using standard heavy impact sources*, Japanese Industrial Standard, 2019.

[27] K. Hook, J. Cheer, and S. Daley, "A parametric study of an acoustic black hole on a beam," *The Journal of the Acoustical Society of America*, vol. 145, no. 6, pp. 3488–3498, 2019.

[28] X. Li and D. Qian, "Sound radiation of a beam with a wedge-shaped edge embedding acoustic black hole feature," *Journal of Sound and Vibration*, vol. 439, pp. 287–299, 2019, ISSN:

0022460X. DOI: 10.1016/j.jsv.2018.10.009. [Online]. Available: https://linkinghub.elsevier.com/retrieve/pii/S0022460X1830676X.

[29] C. Qian, M. Sylvain, B. Delphine, and N. Juan, "Development of a vibroacoustic stochastic finite element prediction tool for a clt floor," *Applied Sciences*, vol. 9, p. 1106, 6 2019, ISSN: 2076-3417. DOI: 10.3390/app9061106. [Online]. Available: https://www.mdpi.com/2076-3417/9/6/1106.

[30] L. Tang and L. Cheng, "Periodic plates with tunneled acoustic-black-holes for directional band gap generation," *Mechanical Systems and Signal Processing*, vol. 133, p. 106 257, 2019.

[31] P. Zhao, "Impact sound insulation performance of floating floor assemblies on mass timber slabs," M.S. thesis, University of British Columbia, 2019. DOI: 10.24124/2022/59324.

[32] T. C. : I. 4. 2, *Rating of sound insulation in buildings and of building elements*, 2020. [Online]. Available: https://www.iso.org/standard/77435.html.

[33] T. C. : I. 4. 2, *Rating of sound insulation in buildings and of building elements. part2: Impact sound insulation*, 2020. [Online]. Available: https://www.iso.org/standard/69867.html.

[34] o. B. Canadian Commission and F. Codes, "National building code of canada: 2020," no. 978-0-660-37913-5, 2020. DOI: 10.4224/w324-hv93.

[35] G. =. Gouvernement du Québec, "Policy for the use of wood in construction," 2020. [Online]. Available: https://www.quebec.ca/agriculture-environnement-et-ressources-naturelles/forets/entreprises-industrie/soutien-industrie-forestiere/politique-dintegration-du-bois-en-construction.

[36] A. Pelat, F. Gautier, S. C. Conlon, and F. Semperlotti, "The acoustic black hole: A review of theory and applications," *Journal of Sound and Vibration*, vol. 476, p. 115 316, 2020.

[37] N. Wang, H. Ji, C. Zhang, Y. Lu, J. Qiu, and L. Cheng, "A new type of two-dimensional acoustic black hole-based vibration absorber," in *INTER-NOISE and NOISE-CON Congress and Conference Proceedings*, Institute of Noise Control Engineering, vol. 261, 2020, pp. 5300–5310.

[38] Y. Yang, F. Chiaki, K. Michael, and M. Brian, "Analysis of the vibroacoustic characteristics of cross laminated timber panels using a wave and finite element method," *Journal of Sound and Vibration*, vol. 494, p. 115 842, 2021, ISSN: 0022460X. DOI: 10.1016/j.jsv.2020.115842. [Online]. Available: https://linkinghub.elsevier.com/retrieve/pii/S0022460X20306714 (visited on 03/2021).

[39] J. Deng, O. Guasch, L. Maxit, and N. Gao, "A metamaterial consisting of an acoustic black hole plate with local resonators for broadband vibration reduction," *Journal of Sound and Vibration*, vol. 526, p. 116 803, 2022.

[40] B. Gibson, N. Tuan, S. Sina, H. David, and N. Tuan, "The low frequency structure-borne sound problem in multi-storey timber buildings and potential of acoustic metamaterials: A review," *Building and Environment*, vol. 224, p. 109 531, 2022, ISSN: 03601323. DOI: 10.1016/j.buildenv.2022.109531. [Online]. Available: https://linkinghub.elsevier.com/retrieve/pii/S0360132322007612.

[41] M. Mueller-Trapet, S. Skoda, Y.-J. Choi, I. Batista da Cunha, and J. Mahn, "Noise from above: A summary of studies regarding the perceived annoyance due to impact sounds," *The Journal of the Acoustical Society of America*, vol. 152, no. 4, A66–A66, 2022.

[42] S. Schoenwald and S. Vallely, "Cross laminated timber elements with functional grading and localised ballast to improve airborne and impact sound insulation," 2023.